















The TRAPPIST-1 Habitable Atmosphere Intercomparison (THAI). Part III: Simulated Observables – The return of the spectrum

1 THOMAS J. FAUCHEZ ^{1,2,3} GERONIMO L. VILLANUEVA ¹ DENIS E. SERGEEV ⁴ MARTIN TURBET ^{5,6}
2 IAN A. BOUTLE ^{7,8} KOSTAS TSIGARIDIS ^{9,10} MICHAEL J. WAY ^{10,3,11} ERIC T. WOLF ^{12,13,3}
3 SHAWN D. DOMAGAL-GOLDMAN ^{1,3,13} FRANÇOIS FORGET ⁶ JACOB HAQQ-MISRA ^{13,14} RAVI K. KOPPARAPU ^{1,3,13}
4 JAMES MANNERS ^{7,15} AND NATHAN J. MAYNE ⁸

5 ¹NASA Goddard Space Flight Center, 8800 Greenbelt Road, Greenbelt, MD 20771, USA

6 ²Goddard Earth Sciences Technology and Research (GESTAR), Universities Space Research Association (USRA), Columbia, MD 7178,
7 USA

8 ³NASA GSFC Sellers Exoplanet Environments Collaboration

9 ⁴Department of Mathematics, College of Engineering, Mathematics, and Physical Sciences, University of Exeter Exeter, EX4 4QF, UK

10 ⁵Observatoire Astronomique de l'Université de Genève, Université de Genève, Chemin des Maillettes 51, 1290 Versoix, Switzerland.

11 ⁶Laboratoire de Météorologie Dynamique/IPSL, CNRS, Sorbonne Université, École Normale Supérieure, PSL Research University, École
12 Polytechnique, 75005 Paris, France

13 ⁷Met Office, FitzRoy Road, Exeter, EX1 3PB, UK

14 ⁸Department of Astrophysics, College of Engineering, Mathematics, and Physical Sciences, University of Exeter, Exeter, EX4 4QL, UK

15 ⁹Center for Climate Systems Research, Columbia University, New York, NY, USA

16 ¹⁰NASA Goddard Institute for Space Studies, 2880 Broadway, New York, NY 10025, USA

17 ¹¹Theoretical Astrophysics, Department of Physics and Astronomy, Uppsala University, Uppsala, Sweden

18 ¹²Laboratory for Atmospheric and Space Physics, University of Colorado Boulder, Boulder, CO, USA

19 ¹³NASA NExSS Virtual Planetary Laboratory, Seattle, WA, 98195, USA

20 ¹⁴Blue Marble Space Institute of Science, Seattle, WA, USA

21 ¹⁵Global Systems Institute, University of Exeter, Exeter, EX4 4QF, UK

22 (Received; Revised; Accepted)

23 Submitted to PSJ

24 ABSTRACT

25 The TRAPPIST-1 Habitable Atmosphere Intercomparison (THAI) is a community project that aims
26 to quantify how differences in general circulation models (GCMs) could impact the climate prediction
27 for TRAPPIST-1e and, subsequently its atmospheric characterization in transit. Four GCMs have
28 participated in THAI so far: ExoCAM, LMD-Generic, ROCKE-3D and the UM. This paper, focused
29 on the simulated observations, is the third part of a trilogy, following the analysis of two land planet
30 scenarios (part I) and two aquaplanet scenarios (part II). Here, we show a robust agreement between the
31 simulated spectra and the number of transits estimated to detect the land planet atmospheres. For the
32 cloudy aquaplanet ones, a 5- σ detection of CO₂ could be achieved in about 10 transits if the atmosphere
33 contains at least 1 bar of CO₂. That number can vary by 41–56% depending on the GCM used to
34 predict the terminator profiles, principally due to differences in the cloud deck altitude, with ExoCAM
35 and LMD-G producing higher clouds than ROCKE-3D and UM. Therefore, for the first time, this
36 work provides “GCM uncertainty error bars” of $\sim 50\%$ that need to be considered in future analyses
37 of transmission spectra. We also analyzed the inter-transit variability induced by weather patterns
38 and changes of terminator cloudiness between transits. Its magnitude differs significantly between the
39 GCMs but its impact on the transmission spectra is within the measurement uncertainties. THAI has
40 demonstrated the importance of model intercomparison for exoplanets and also paved the way for a
41 larger project to develop an intercomparison meta-framework, namely the Climates Using Interactive
42 Suites of Intercomparisons Nested for Exoplanet Studies (CUISINES).

43 1. INTRODUCTION

Here at last... comes the end of our fellowship. I will not say do not weep, for not all tears are an evil.

—J.R.R. Tolkien, *The Return of the King*

44 At the dawn of terrestrial exoplanet atmospheric characterization with the James Webb Space Telescope (JWST),
 45 predicting the detectability of the atmospheres of such planets is crucial in order to prepare for observations and
 46 maximize the scientific return. JWST Guaranteed Time Observations (GTO) and Cycle 1 proposals have already
 47 been selected. While CO₂ can be potentially detectable from Cycle 1, it is unlikely that enough transits would be
 48 accumulated for any single target to characterize in-depth the atmosphere of a terrestrial exoplanet (Fauchez et al.
 49 2019; Lustig-Yaeger et al. 2019; Pidhorodetska et al. 2020) in the Habitable Zone (HZ; see e.g. Kopparapu et al. 2013)
 50 of M-dwarf stars. The presence of CO₂ has been shown to be the best proxy (Fauchez et al. 2019; Lustig-Yaeger
 51 et al. 2019; Turbet et al. 2020) for the detection of a potentially habitable atmosphere due to its strong absorption
 52 band in the mid-infrared (MIR) at 4.3 μm and in the far-infrared at $\sim 15 \mu\text{m}$. However a 5- σ detection under
 53 cloudy conditions would likely require more than a dozen transits, even for the most favorable HZ terrestrial planet,
 54 TRAPPIST-1e (Fauchez et al. 2019).

55
 56 TRAPPIST-1e belongs to the seven small transiting planet system TRAPPIST-1 (Gillon et al. 2016, 2017; Luger et al.
 57 2017) at 12.0 pc away. The star, TRAPPIST-1, is a M8V just slightly larger than Jupiter which makes it very suitable
 58 for transmission spectroscopy of the atmosphere of small rocky planets. Indeed, the ratio of the surface area of the star's
 59 disk blocked out by the planet's disk (including its atmosphere), i.e. the transit depth, is inversely proportional to the
 60 square of the star radius. Also, around such a cold and dim star, HZ planets have a very short orbital period leading to
 61 very frequent transits and therefore more accessible data on their atmospheres. The Hubble Space Telescope (HST) has
 62 been used to infer the presence of an atmosphere on TRAPPIST-1e and its sibling planets (de Wit et al. 2016, 2018).
 63 However, the precision of HST data were only able to either be consistent with the absence of an atmosphere or to rule
 64 out clear-sky H₂ dominated atmospheres while Moran et al. (2018) showed that HST observations could actually be
 65 fit by cloudy/hazy H₂ atmospheres. Yet, the comparison of TRAPPIST-1e bulk density measurements (Grimm et al.
 66 2018; Agol et al. 2021) to H₂-rich planets mass-radius relationships (Turbet et al. 2020) along with atmospheric escape
 67 modelling and gas accretion modelling (Hori & Ogihara 2020) provide accumulating evidence against the presence of
 68 H₂ dominated cloudy atmospheres around TRAPPIST-1 planets, including TRAPPIST-1e (see Turbet et al. 2020 and
 69 references therein). Furthermore, Krishnamurthy et al. (2021) reported strong upper limit constraints on the absence
 70 of helium in the atmosphere of TRAPPIST-1e. More in-depth knowledge about the absence or presence of a high mean
 71 molecular weight atmosphere on TRAPPIST-1e would most likely require JWST transit observations. Indeed, even
 72 some of the largest planned optical telescope (Extremely Large Telescopes, ELTs) are unable — even at the diffraction
 73 limit — to separate the light from TRAPPIST-1 and its planets, because of their very small angular separation.
 74 The same is true for future space observatories such as the Roman (Douglas et al. 2020), Large UV/Optical/Infrared
 75 Surveyor (LUVOIR, TheLUVOIRTeam (2019)), the Habitable Exoplanet Observatory HabEx (Gaudi et al. (2018))
 76 for which the inner working angle of their coronagraph would block the light not only from the star but from the
 77 entire system. Also, in the HZ, the planet is relatively too cold to significantly emit thermal infrared radiation which
 78 makes it very challenging to characterize its emission spectrum (Fauchez et al. 2019; Lustig-Yaeger et al. 2019; Kane
 79 et al. 2021); more close-in planets, however, will be more sensitive to this technique (Morley et al. 2017; Lustig-Yaeger
 80 et al. 2019; Koll et al. 2019; Turbet et al. 2020). Orbital broadband phase-dependent variations in the combined
 81 planetary thermal emission and reflected stellar energy can also provide clues about the atmospheric structure and
 82 surface properties of the planet (e.g. Selsis et al. 2011; von Paris et al. 2016; Koll & Abbot 2016; Turbet et al. 2016;
 83 Haq-Misra et al. 2018; Wolf et al. 2019), but the level of the phase variation of part-per-billion (ppb) are far beyond
 84 our current instrumental capabilities (Wolf et al. 2019). Atmospheric characterization of TRAPPIST-1e may be also
 85 possible from the ground (Wunderlich et al. 2020) with the planned European Extremely Large Telescope (E-ELT),
 86 but this demonstration has been done assuming a clear-sky TRAPPIST-1e atmosphere, which may have led to an
 87 over-estimation of the E-ELT's capabilities.

88 Therefore, JWST transit observations are the most viable atmospheric characterization technique for the
 89 TRAPPIST-1 planets in the coming decade. Several studies have used either GCMs (Fauchez et al. 2019; Pidhorodetska
 90 et al. 2020; May et al. 2021) or 1-D radiative convective climate models coupled to photochemistry (Lincowski
 91 et al. 2018; Lustig-Yaeger et al. 2019; Wunderlich et al. 2019, 2020; Lin et al. 2021) or analytical models (Morley

et al. 2017) to predict the detectability of standard atmospheres such as the modern Earth, the Archean Earth or a CO₂-dominated atmosphere. While these predictions inherently vary from one model category to another due to for instance the day/night contrast or the presence of clouds and hazes in the simulated atmosphere, models in the same category may also disagree due to, for example, differences in the atmospheric profiles at the terminator. Evaluating these differences and their impact on synthetic observations in order to optimize JWST observation strategies are the core objectives of the TRAPPIST-1 Habitable Atmosphere Intercomparison (THAI; Fauchez et al. 2020a, 2021). The comparison of these simulated climate systems are described in the companion papers (Turbet et al. 2021, referred to as Part I) for the dry planet benchmark scenarios (Ben 1 & Ben 2) and in (Sergeev et al. 2021, referred to as Part II) for the aquaplanet (Hab 1 & Hab 2) scenarios. The paper is structured as follows: In Section 2 the methods and tools used in this study are described. In Section 3, we present the simulated transmission spectra using each of the GCM outputs, using both time average and time dependent terminator profiles. Finally, conclusions are given in Section 4.

2. METHOD

2.1. *The THAI GCM simulations*

In this paper, Part III of a trilogy of THAI papers, we use the same GCM simulations that have been extensively analyzed in Part I (Turbet et al. 2021) and Part II (Sergeev et al. 2021), namely the Ben 1 & Ben 2 and Hab 1 & Hab 2 cases, respectively. Briefly, the Ben 1 & Ben 2 cases are dry land planet simulations, while the Hab 1 & Hab 2 cases assume that the surface is fully covered by a global (static) ocean and that there is water vapour and clouds in the atmosphere. Ben 1 & Hab 1 atmospheric composition is broadly similar to that of modern Earth (1 bar of N₂, 400 ppmv of CO₂), while the Ben 2 & Hab 2 experiments assume a CO₂-dominated atmosphere (1 bar). 10 orbits (61 Earth days) at a frequency of 6 h are output for Ben 1 & Ben 2, while 100 orbits (610 Earth days) are output for Hab 1 & Hab 2, in order to smooth out the internal variability with a period of about a dozen of orbits induced by clouds.

Each of these simulations have been performed by the four THAI GCMs: ExoCAM (Wolf et al. 2021) the exoplanet branch of the Community Earth System Model (CESM, <http://www.cesm.ucar.edu/models/cesm1.2/>) version 1.2.1., the LMD Generic model (LMD-G, see e.g. Wordsworth et al. 2011; Turbet et al. 2018), the Resolving Orbital and Climate Keys of Earth and Extraterrestrial Environments with Dynamics (ROCKE-3D Way et al. 2017)) and the Met Office Unified Model (the UM, see e.g. Mayne et al. 2014; Boutle et al. 2017). More details on these four GCMs are also provided in the THAI protocol (Turbet et al. 2021; Sergeev et al. 2021) and the THAI workshop report (Fauchez et al. 2021).

2.2. *Simulated Spectra*

We use the Planetary Spectrum Generator (PSG, Villanueva et al. 2018; ?) to simulate transmission spectra of TRAPPIST-1e for each of the THAI scenarios, using data from each of the four GCMs. PSG is an online radiative transfer tool that can be used to simulate planetary spectra observations from any ground or space-based observatory for various objects of the solar system and beyond, and it also includes a noise calculator.

To simulate and compare time-averaged transmission spectra across the models, we first average the atmospheric properties over the 10 orbits of Ben 1 & Ben 2 and over the 100 orbits of Hab 1 & Hab 2. For our transit calculations, atmospheric profiles were created for each GCM lat × lon cell at the terminator of the planet using abundance, pressures, temperatures as reported by the GCM for that specific terminator cell (vertical parameters of that cell). Then transit spectra were computed using those profiles across all terminator cells, and the total transit spectrum was computed by the average of all transits across the terminators (weighted the area of the cell).

Specifically, the radiative transfer is computed employing a layer-by-layer pseudo-spherical refractive raytracing algorithm. Rayleigh cross-sections are computed as a summation of the individual molecular cross-sections (Villanueva et al. 2022; Snee & Ubachs 2005), which are computed at each wavelength based on the polarizability of the encompassing molecules. PSG employs polarizability values as compiled on the Computational Chemistry Comparison and Benchmark DataBase at NIST (<https://cccbdb.nist.gov/pollistx.asp>). Collision-induced absorptions (CIA) generated by inelastic collisions of molecules in a gas are included from considering the latest HITRAN CIA compilations (Gordon et al. 2022) and the HITRAN CIA database (Karman et al. 2019), as well as several other sources as reported in (Villanueva et al. 2022), including the MT-CKD water continuum (v3.5, Kofman & Villanueva (2021)). In the presented spectral range and assumed background abundance, only these CIAs contain notable signatures: CO₂–CO₂, H₂O–H₂O, H₂O–N₂, N₂–N₂. Molecular absorptions were included via by correlated-k tables based on

the latest HITRAN 2020 linelist (Gordon et al. 2022), which were complemented at short wavelengths ($< 1 \mu m$) with UV cross-sections, primarily from the MPI Mainz UV/VIS Spectral Atlas (Keller-Rudek et al. 2013). Aerosols properties are modelled following Mie theory, with water cloud scattering properties as described in Massie & Hervig (2013) while the ice cloud optical property parameterization uses Warren (1984), as also described in Massie & Hervig (2013). The partial abundance of the aerosols at the grid-box is explicitly defined by the GCM kg/kg profile at that location, meaning that a profile with zero abundance would correspond to a fully clear scenario. An average of all these spectra is then computed to obtain a limb-averaged spectra as it would be observed by an instrument. Detailed information regarding the computation of correlated-k tables, Rayleigh scattering, the treatment of CIAs, MT_CKD, the ray tracing algorithm, and the radiative-transfer method can be found in (Villanueva et al. 2022).

2.3. Instruments, noise and number of transits

2.3.1. Instruments

We have simulated JWST observations of TRAPPIST-1e transiting its host star. JWST is a 6.5 m tip-to-tip segmented telescope, equivalent to a full circular aperture of 5.6 m of diameter. Previous studies have showed that the NIRSpec Prism (covering the $0.6 - 5.3 \mu m$ region at resolving power $R=100$) is the JWST instrument most adapted to characterize the atmosphere of temperate terrestrial planets (Fauchez et al. 2019; Lustig-Yaeger et al. 2019; Pidhorodetska et al. 2020; Wunderlich et al. 2020). Indeed, this spectral region contains various molecular signatures of interest such as O_2 , O_3 , H_2O , NO_2 , N_2O , CH_4 , CO and CO_2 . The latter may likely be the only one with a strong enough absorption features to be detectable with JWST in a reasonable number of transits (i.e. achievable in 5 JWST cycles assuming a constant 4 transit observation per cycle as in Cycle 1), when clouds and hazes are present in the atmosphere. It has therefore been suggested as the best proxy to detect the atmosphere of habitable planets (Fauchez et al. 2019; Turbet et al. 2020). Note that JWST Guaranteed Time Observations (GTO) proposals have already been awarded for the NIRSpec instrument that will attempt molecular detection with four transit observations (program 1331). In this work we compute spectra from 0.6 to $20 \mu m$, across the range of both JWST NIRSpec Prism and MIRI medium-resolution spectrometer (MRS) and present the figures at $R=100$ offering the best visibility for multiple spectrum plots. Signal-to-noise ratios (S/N) and number of transit estimations are only presented for NIRSpec Prism.

2.3.2. Noise

2.3.3. Estimation of the detectability of the atmosphere — identical transits

First, we computed noise estimates with PSG, and validated these by employing the official JWST Exposure Time Calculator, obtaining very good agreement. For NIRSpec Prism, the effective spectral resolution is $0.022 \mu m$. We have selected the clear filter with the sub-array SUB512S and the rapid readout pattern with two groups per integration and 0.225 s per frame. This leads to a partial saturation near the peak of the Stellar Energy Distribution (SED) following (Batalha et al. 2018; Lustig-Yaeger et al. 2019). For MIRI LRS, the effective resolution is $0.0654 \mu m$, and we selected the P750L disperser with the sub-array SLITLESSPRISM, and a FASTR1 readout pattern with 20 groups per integration with a frame time of 0.15 s.

We assumed a transit time of 3345 s (0.93 h) (Agol et al. 2021). To take into account the noise of the out-of-transit baseline, we used JWST NIRSpec GTO proposal 1331 (Lewis et al. 2018) for which each transit event will be observed for ~ 4 hours, therefore leading to an out-of-transit observation of $\sim 3 \times$ transit duration. As the noise adds in quadrature, the single transit noise N , including a $3 \times$ out-of-transit baseline is computed as follow:

$$\begin{aligned}
 N &= \sqrt{N_{out}^2 + N_{in}^2} \\
 &= \sqrt{(1/time_{out})^2 + (1/time_{in})^2} \\
 &= \sqrt{(1/3)^2 + (1/1)^2} \\
 &= \sqrt{4/3}
 \end{aligned} \tag{1}$$

To estimate the 1 transit S/N of CO_2 across the NIRSpec Prism range ($0.6-5.3 \mu m$) and the number of transits required to achieve a $5\text{-}\sigma$ detection of CO_2 we proceed following the list below:

1. We compute the spectrum without CO_2
2. We compute the spectrum with CO_2

- 173 3. We compute the difference between step 1. and 2 across the whole instrument range
 174 4. We compute the S/N by dividing step 3. by the noise for 1 transit (3345 s) in each spectral interval.
 175 5. We apply the $\sqrt{4/3} = 1.155$ factor to the noise to take into account the out-of-transit noise.
 176 6. The S/N of CO₂ across the whole instrument range then computed following ? as:

$$S/N = \sqrt{\sum_{i=0}^n S/N_i^2} \quad (2)$$

176 where S/N_i are the individual S/N in each spectral interval.

- 177 7. From the S/N, the number of transits N_t required to achieve a 5- σ detection is done as following [Fauchez et al. \(2019\)](#); [Fauchez et al. \(2020b\)](#):

$$N_t = \left(\frac{5}{S/N} \right)^2 \quad (3)$$

177 3. TRANSMISSION SPECTRA

178 3.1. Ben 1 & Ben 2 cases (dry planets)

179 In Fig. 1 and 2 we can see the transmission spectra simulated with PSG using the atmospheric profiles of THAI cases
 180 Ben 1 & Ben 2, respectively, provided by each GCM. In the panel A) of both figures, the lowest pressures (highest
 181 altitudes) used to compute the spectra correspond to the top of the modelled domains, which are 10^{-5} , 4×10^{-5} ,
 182 14×10^{-5} and 4×10^{-5} bar for Ben 1 and 10^{-5} , 4×10^{-5} , 14×10^{-5} and 13×10^{-5} bar for Ben 2 for ExoCAM, LMD-G,
 183 ROCKE-3D and the UM, respectively. Note that most GCMs have the domain lid at relatively high pressures for
 184 numerical stability reasons and as moving it to lower pressures require taking into account complex upper atmospheric
 185 processes such as non-local thermodynamic equilibrium, molecular diffusion, etc (see [Fauchez et al. \(2021\)](#), section
 186 4.1). The lowest pressures usually correspond to a top-of-atmosphere (TOA) altitude of 50 to 70 km for Earth-like
 187 simulations. However, the pressure at this altitude is usually too high to fully capture the transmitted light through
 188 the planet's atmosphere and the strongest atmospheric features can be truncated. This is clearly seen in the Ben 2
 189 case where the CO₂ strongest absorption lines are truncated (Fig. 2a). To bypass this limitation, we used PSG to
 190 extend the atmosphere to much lower pressures, assuming an isothermal profile and constant volume mixing ratios for
 191 the dry gases. This is similar to the so-called "ghost layer" used in [Amundsen et al. \(2016\)](#). We have estimated the
 192 TOA pressure that would fully resolve the spectral lines for Ben 1 & Ben 2 as 10^{-7} and 10^{-10} bar, respectively. Lower
 193 pressures are required for Ben 2 because the opacity of a pure CO₂ atmosphere remains strong at lower pressures than
 194 that of a N₂-dominated atmosphere.

195 Using the data with extrapolated model top, we have estimated the number of transits that would be required to
 196 detect such atmospheres with a 5- σ confidence level as presented in Table 1. Two estimations are shown, the first one
 197 uses the method presented in section 2.3.2 and is referred to as 5 σ Transits. The second method only uses the CO₂ line
 198 at 4.3 μm as done in ([Fauchez et al. 2019](#); [Wunderlich et al. 2019](#); [Pidhorodetska et al. 2020](#)) and is referred to as 5 σ
 199 Transit-4.3 μm . Also shown are the signal-to-noise ratio for 1 transit (S/N-1) and four transits (S/N-1), corresponding
 200 to JWST Cycle 1 TRAPPIST-1e transit observation (GTO Proposal 1331 by PI Nikole Lewis, [Lewis et al. \(2017\)](#)).

201 First, we can see that for a Ben 1 atmosphere, an average of 2.6 σ could be achieved from Cycle 1 while an average
 202 of 4.3 σ could be achieved for a Ben 2 atmosphere with more CO₂. To reach the necessary 5- σ threshold, an average
 203 of 17 and 6 transits would be needed for Ben 1 and Ben 2, respectively. When using only the CO₂ line at 4.3 μm
 204 these numbers go up to 24 and 25 transits, respectively, demonstrating that this method strongly over-estimate the
 205 number of necessary transits, especially if the amount of CO₂, and therefore the number of strong lines, is high. The
 206 inter-model differences for 5- σ Transit are small in both cases, the maximum difference between the GCMs being
 207 24 % and 33 % for Ben 1 and Ben 2, respectively demonstrating that the four GCMs provide similar atmospheric
 208 profiles at the terminator to provide consistent simulated spectra and expected number of transits to detect a dry
 209 1 bar atmosphere with a relatively high mean molecular weight. Note that we did not consider the spectral impact of
 210 dust that can be lifted from the surface of a land planet and persist in the atmosphere. Dust would likely raise the
 211 continuum level, thereby decreasing the amplitude of each spectral line as shown in [Boutle et al. \(2020\)](#). The expected
 212 effect would be of the order of 10 ppm.

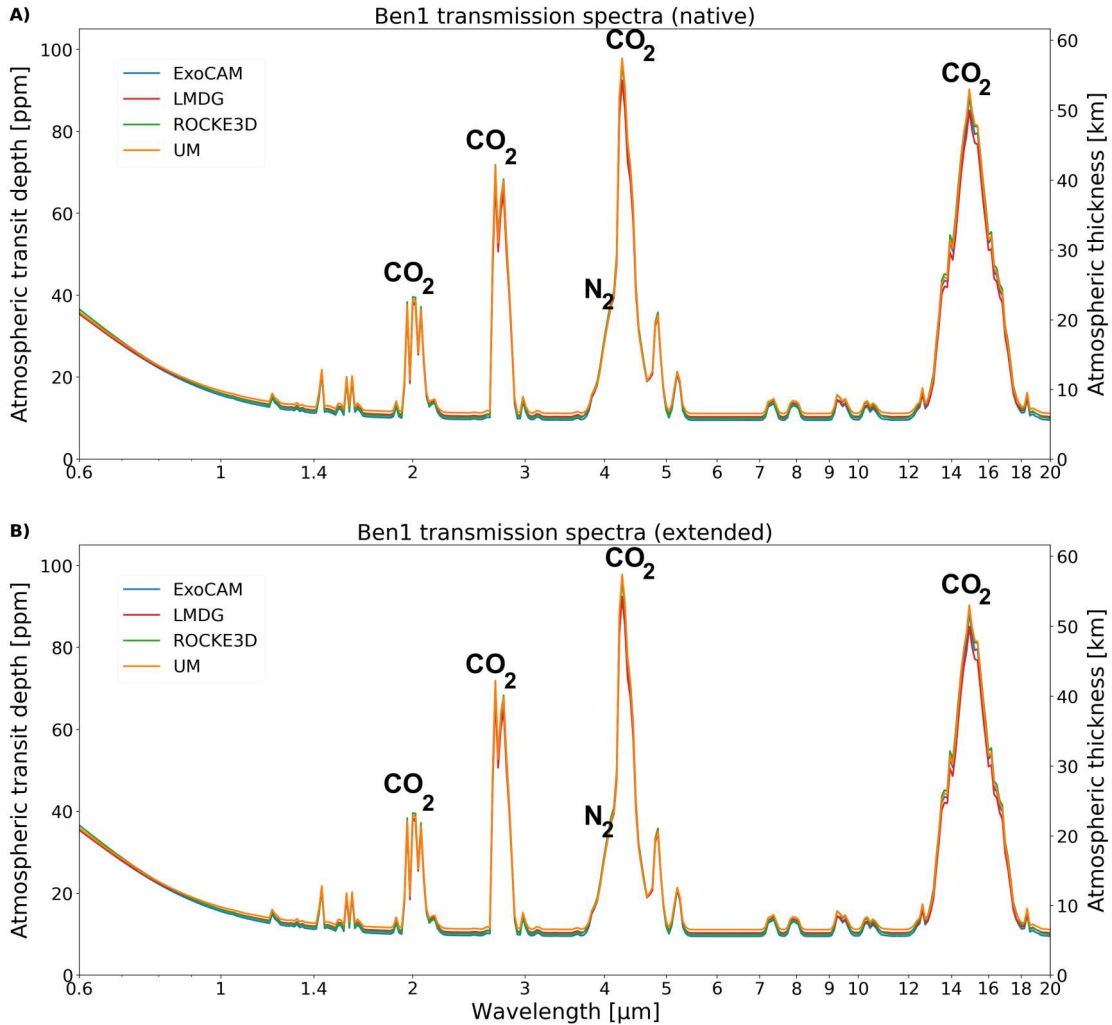


Figure 1. Ben 1 transmission spectra simulated with PSG using the terminator atmospheric profiles from the ExoCAM, LMD-G, ROCKE-3D and the UM simulations. In Panel A) the atmospheric profiles are limited up to the lowest pressure at the top of the GCMs, namely 10^{-5} , 4×10^{-5} , 14×10^{-5} and 4×10^{-5} bar for ExoCAM, LMD-G, ROCKE-3D and UM, respectively while in Panel B) the atmospheric profiles have been extended up to 10^{-7} bar assuming an isothermal atmosphere and fixed mixing ratios for the dry gases. The differences between the transmission spectra are extremely small.

3.2. Hab 1 & Hab 2 cases (aquaplanets)

Rocky exoplanets in the HZ and with surface liquid water will likely have water in a vapor and condensed form in the atmosphere. Clouds have been shown to severely impede atmospheric characterization via transmission spectroscopy (Fauchez et al. 2019; Komacek et al. 2020; Suissa et al. 2020a). Furthermore, clouds are notoriously difficult to represent correctly in GCMs, because the characteristic timescale and size of individual clouds is too small to be simulated explicitly and they involve a tremendous amount of physical processes. GCMs thus rely on sub-grid scale parameterizations to represent the formation of clouds that can significantly differ between models (Sergeev et al. 2021). These discrepancies can then lead to different predicted surface temperatures, as was noted in exoplanet GCM simulations by Yang et al. (2019). Details on the differences in GCM predictions, especially for clouds, are given in the companion paper (Sergeev et al. 2021).

Here, we use PSG to compute transmission spectra for both the Hab 1 & Hab 2 cases. The atmospheric properties at the terminator have been time averaged over the 100 orbits in order to smooth out variability that can be introduced by weather patterns and change in clouds at the terminator, as is commonly done for such planets (Fauchez et al.

213

214

215

216

217

218

219

220

221

222

223

224

225

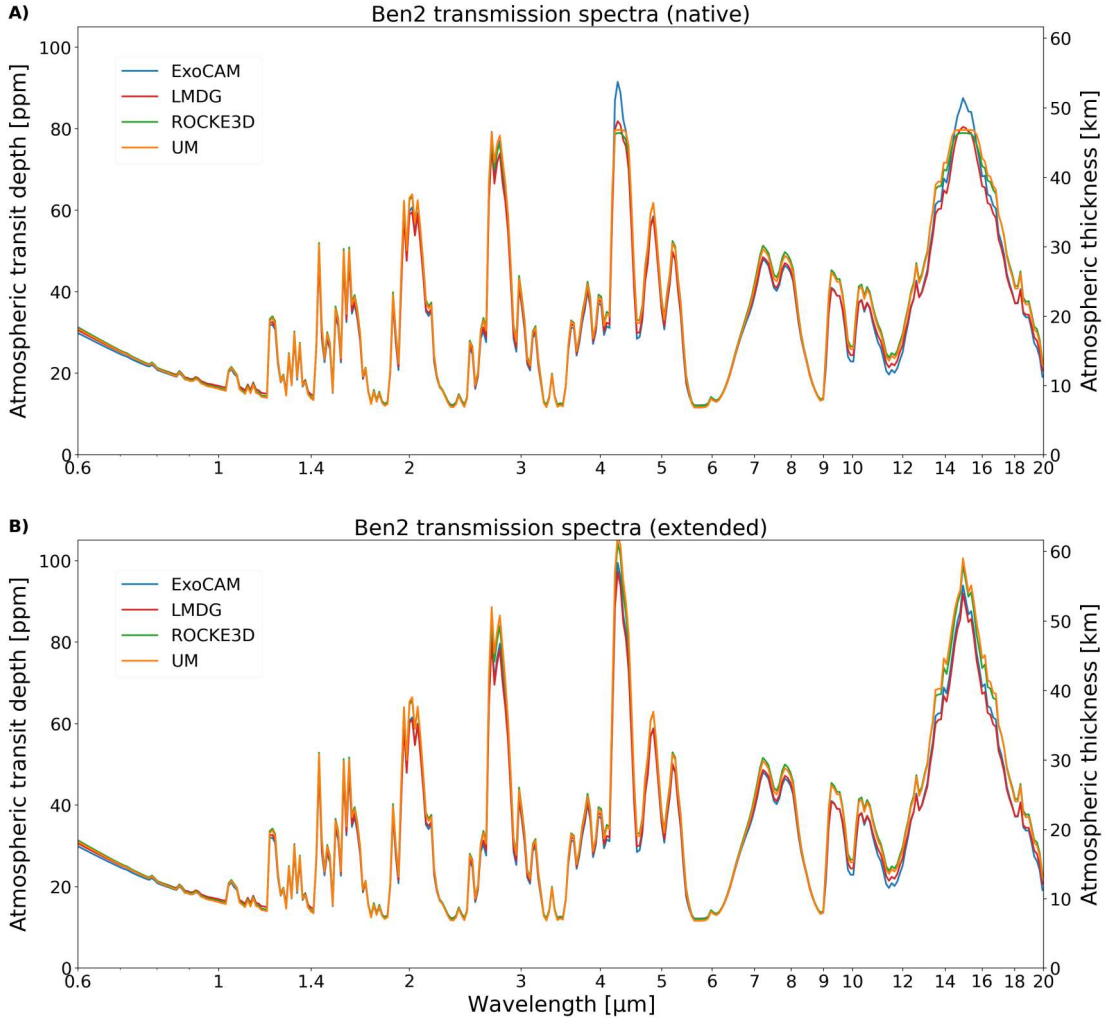


Figure 2. Ben 2 transmission spectra simulated with PSG using the terminator atmospheric profiles from the ExoCAM, LMD-G, ROCKE-3D and UM simulations. In Panel A) the atmospheric profiles are limited up to the lowest pressure at the top of the GCMs, namely 10^{-5} , 4×10^{-5} , 14×10^{-5} and 13×10^{-5} bar for ExoCAM, LMD-G, ROCKE-3D and the UM, respectively while in Panel B) the atmospheric profiles have been extended up to 10^{-10} bar assuming an isothermal atmosphere and fixed mixing ratios for the dry gases. CO₂ features are truncated if the atmospheres are not vertically extended. Visible differences between the spectra appear in the CO₂ bands in both the native (panel A) and extended (panel B) scenarios. CO₂ labels are not shown as the spectra are exclusively CO₂.

226 2019; Komacek et al. 2020; Pidhorodetska et al. 2020; Suissa et al. 2020a,b). Details on the impact of atmospheric
 227 variability on transmission spectra are given in Sec. 3.3.

228 Fig. 3 shows the Hab 1 transmission spectra calculated using the output from ExoCAM, LMD-G, ROCKE-3D and
 229 the UM. The extension of the top of the model has a negligible impact on the spectra, except within the strongest
 230 $4.3 \mu\text{m}$ and $15 \mu\text{m}$ CO₂ absorption bands. The differences between the spectra from the different GCMs are mostly
 231 noticeable in the continuum and for the weakest absorption bands. Indeed, as already shown by Fauchez et al. (2019)
 232 and Suissa et al. (2020a), the continuum level in a cloudy atmosphere is raised to the altitude of the cloud deck.
 233 Strong bands like CO₂ at $4.3 \mu\text{m}$ are less affected by clouds because even if the denser, most absorbing part of the
 234 atmosphere is under them, the efficiency of absorption is so strong that the small CO₂ partial pressure remaining
 235 above the cloud deck is large enough to saturate the line. The ExoCAM continuum level is the highest, followed by
 236 LMD-G, ROCKE-3D and the UM. This is explained by the fact that the liquid water cloud mixing ratio and the
 237 altitude of the cloud deck at the west and east terminators, respectively, are much higher in ExoCAM than in LMD-G,
 238 ROCKE-3D and the UM, in that order (Fig. 4e,f). Regarding ice clouds, while the mixing ratios predicted by each

Table 1. Table summarizing the signal-to-noise ratio achieved from 1 transit (S/N-1), from the four JWST Cycle 1 transits (S/N-4), number of transits to reach a $5\text{-}\sigma$ detection using all available CO_2 lines ($5\text{-}\sigma$ Transit), and using only the $4.3\ \mu\text{m}$ CO_2 line.

Ben1					
Model	S/N-1	S/N-4	$5\text{-}\sigma$ Transit	$5\text{-}\sigma$ Transit- $4.3\mu\text{m}$	
ExoCAM	1.3	2.6	16	23	
LMD-G	1.2	2.4	19	25	
ROCKE-3D	1.3	2.6	15	23	
UM	1.3	2.6	16	23	
Average	1.3	2.6	17	24	
Maximum difference (%)	8	8	24	8	
Ben2					
Model	S/N-1	S/N-4	$5\text{-}\sigma$ Transit	$5\text{-}\sigma$ Transit- $4.3\mu\text{m}$	
ExoCAM	2.2	4.4	5	23	
LMD-G	2.0	4.0	7	28	
ROCKE-3D	2.2	4.4	5	23	
UM	2.2	4.4	5	24	
Average	2.2	4.3	6	25	
Maximum difference (%)	9	9	33	20	
Hab1					
Model	S/N-1	S/N-4	$5\text{-}\sigma$ Transit	$5\text{-}\sigma$ Transit- $4.3\mu\text{m}$	
ExoCAM	0.9	1.8	35	39	
LMD-G	0.9	1.8	29	37	
ROCKE-3D	1.0	2.0	38	31	
UM	1.0	2.0	23	24	
Average	1.0	2.0	29	33	
Maximum difference (%)	10	10	41	45	
Hab2					
Model	S/N-1	S/N-4	$5\text{-}\sigma$ Transit	$5\text{-}\sigma$ Transit- $4.3\mu\text{m}$	
ExoCAM	1.5	3.0	12	36	
LMD-G	1.7	3.4	9	31	
ROCKE-3D	1.7	3.4	8	29	
UM	2.0	4.0	7	23	
Average	1.7	3.4	9	30	
Maximum difference (%)	29	29	56	43	

model are comparable, the average altitude of the clouds is different, with ExoCAM producing the highest ice clouds following by LMD-G, ROCKE-3D and UM (Fig. 4g,h).

Fig. 3 also shows that the LMD-G water band around $6\ \mu\text{m}$ is significantly weaker than that predicted by other models. This is due to the fact that LMD-G simulations have a much drier upper atmosphere (Fig. 4c,d). The amount of water above the tropopause in LMD-G is primarily controlled by the tropopause temperature at the substellar point (where water is injected by deep moist convection) which is the coldest in LMD-G, especially at the western terminator (see the companion paper, [Sergeev et al. 2021](#), Fig. 4). As a result, the detectability of water in Hab 1 simulations for LMD-G is even more challenging than for the other GCMs.

Fig. 5 is the same as Fig. 3, but for Hab 2 simulations. First, we can see that because the CO_2 mixing ratio is much higher in the Hab 2 simulations (from about 400 ppm for Hab 1 to nearly 100 % for Hab 2), strong absorption lines are more easily truncated by a low model top. Similarly to the Hab 1 case, the ExoCAM continuum is higher than that of the other three GCMs. This time, however, the continuum level in ROCKE-3D is slightly above that in LMD-G. Note that LMD-G's absorption peaks are the smallest among the four GCMs.

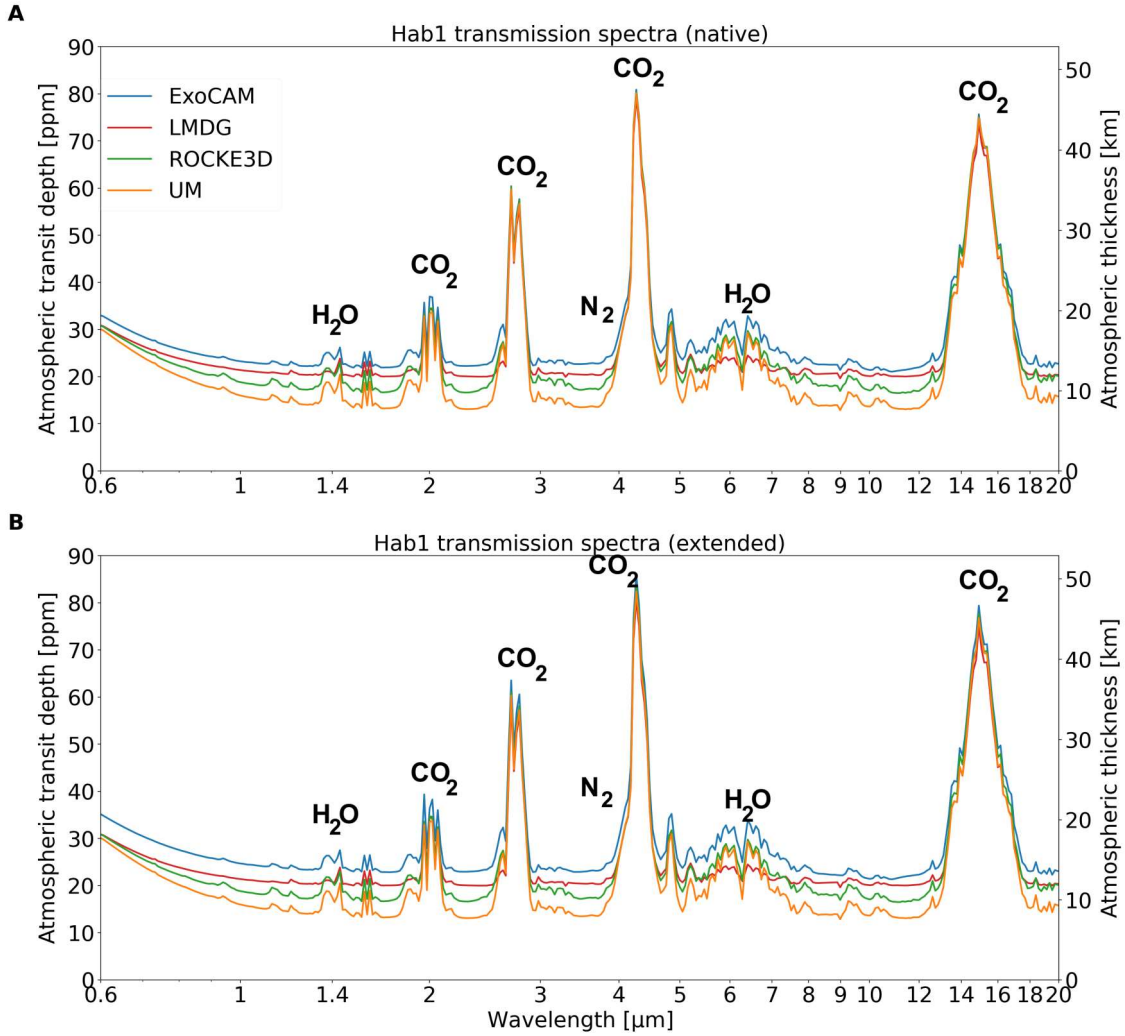


Figure 3. Hab 1 transmission spectra simulated with PSG using the terminator atmospheric profiles from the ExoCAM, LMD-G, ROCKE-3D and the UM simulations. In Panel A) the atmospheric profiles are limited up to the lowest pressure at the top of the GCMs, namely 10^{-5} , 4×10^{-5} , 14×10^{-5} and 4×10^{-5} bar for ExoCAM, LMD-G, ROCKE-3D and the UM, respectively while in Panel B) the atmospheric profiles have been extended up to 10^{-7} bar assuming an isothermal atmosphere and fixed mixing ratios for the dry gases.

252 In the warm and humid atmosphere of the Hab 2 case (Fig. 6a,b) there is no clear temperature inversion at the
 253 tropopause except for a decrease in the lapse rate from 100 hPa and lower (for more details see [Sergeev et al. 2021](#)).
 254 The specific humidity closely follows the temperature profiles: colder temperature profiles correspond to drier profiles
 255 (Fig. 6c,d). Furthermore, the warm atmosphere of Hab 2 results in the liquid water cloud mass mixing ratio being
 256 comparable and even larger than the ice cloud mixing ratio (Fig. 6). When the altitudes of both cloud types are
 257 combined, ExoCAM has on average higher and thicker clouds, followed by ROCKE-3D, then LMD-G and finally the
 258 UM. It is interesting to note that in the warmer, moister and cloudier Hab 2 case, the relative difference in cloudiness
 259 between LMD-G, ROCKE-3D and the UM is smaller than that for Hab 1. Only ExoCAM persistently produces higher
 260 clouds. More detailed discussion about the differences of cloud coverage produced by the THAI models are given in
 261 [Sergeev et al. \(2021\)](#).

262 Similar to the Ben 1 & Ben 2 experiments, we extrapolated the model top for the PSG calculation, which gave the
 263 number of transits required for atmospheric detection with a $5\text{-}\sigma$ confidence level by JWST using the full NIRSpec
 264 Prism spectral range ($5\text{-}\sigma$ Transit) and with the CO₂ line at $4.3 \mu\text{m}$ only ($5\text{-}\sigma$ Transit- $4.3 \mu\text{m}$). For Hab 1, we found
 265 35, 29, 38 and 23 transits, while for Hab 2 we found 12, 9, 8 and 7 transits (for ExoCAM, LMD-G, ROCKE-3D

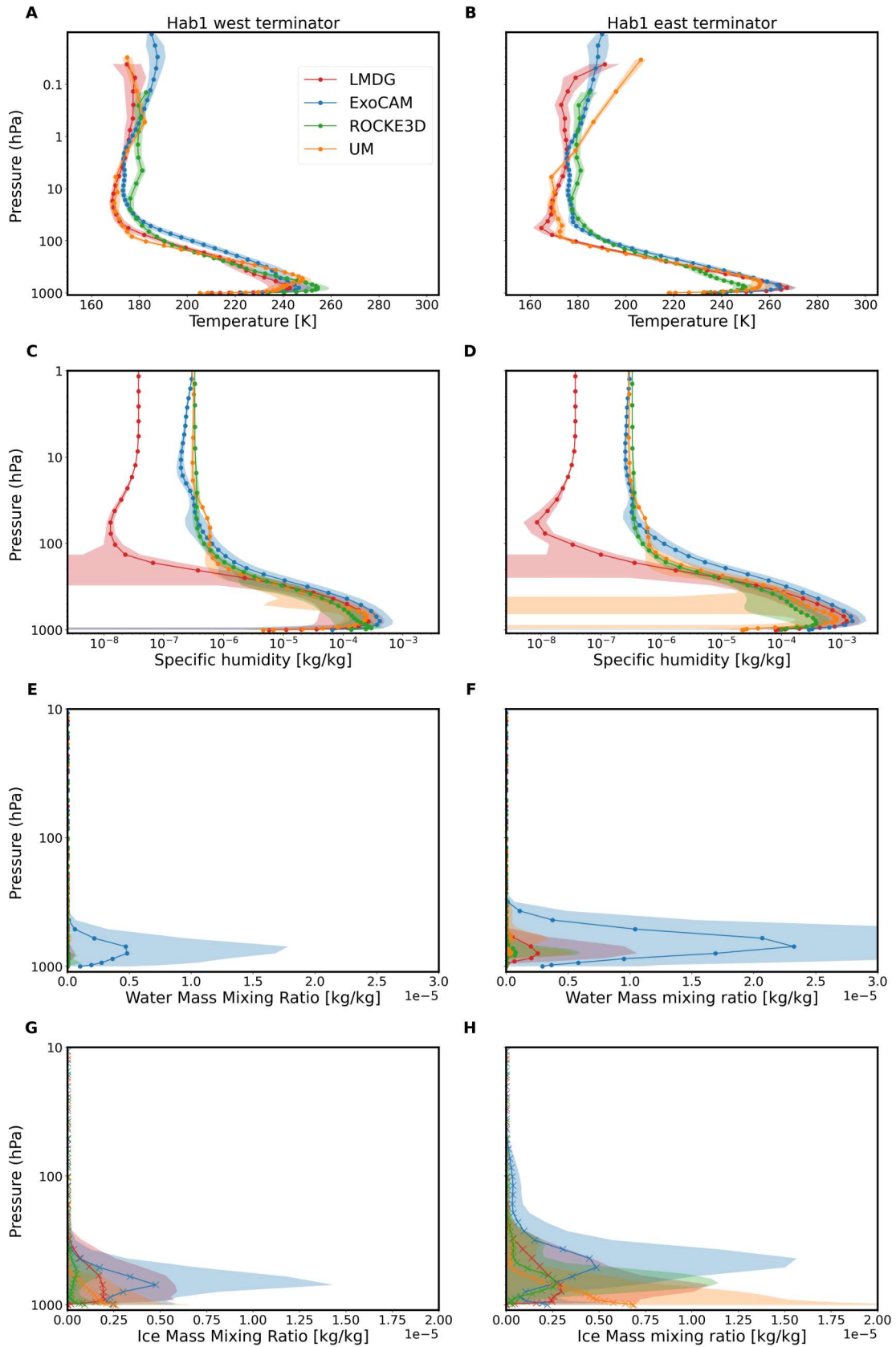


Figure 4. Hab 1 terminator atmospheric profiles predicted by ExoCAM (blue), LMD-G (red), ROCKE-3D (green) and the UM (orange). From top to bottom: temperature, specific humidity, the mass mixing ratio of liquid water and the mass mixing ratio of ice water for the west terminator (left column) and east terminator (right column). Time averaged values are represented by thick lines while the $1 - \sigma$ deviations are represented by shades.

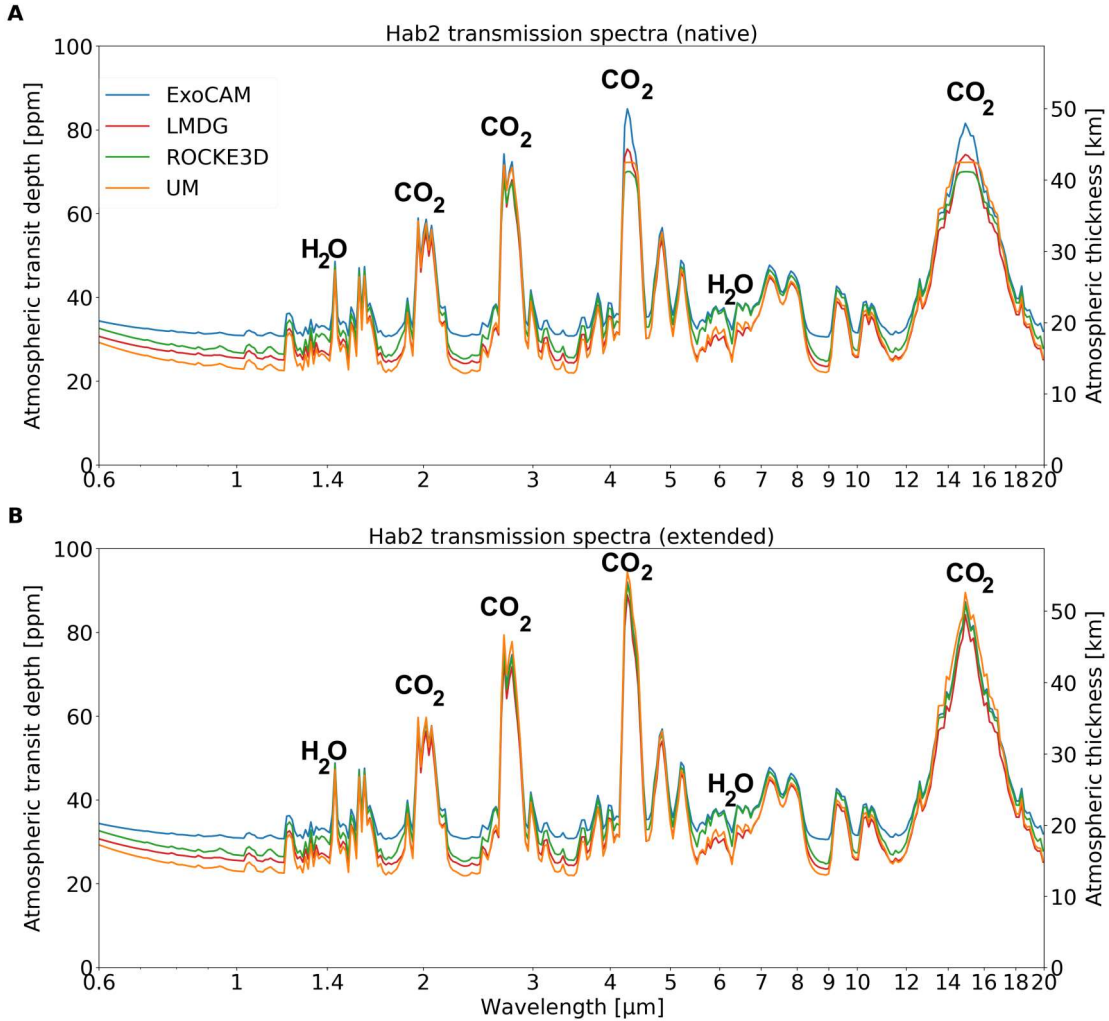


Figure 5. Hab 2 transmission spectra simulated with PSG using the terminator atmospheric profiles from the ExoCAM, LMD-G, ROCKE-3D and the UM simulations. In Panel A) the atmospheric profiles are limited up to the lowest pressure at the top of the GCMs, namely 10^{-5} , 4×10^{-5} , 14×10^{-5} and 13×10^{-5} bar for ExoCAM, LMD-G, ROCKE-3D and UM, respectively while in Panel B) the atmospheric profiles have been extended up to 10^{-10} bar assuming an isothermal atmosphere and fixed mixing ratios for the dry gases. CO_2 features are truncated if the atmospheres are not extended. Differences between the spectra due to clouds are mostly seen in the continuum and for the weakest absorption bands.

266 and UM, respectively). The average number of transits for Hab 1 is 29, with a maximum difference of 41 % and for
 267 Hab 2 it is 9, with a maximum difference of 56 %. Similarly to the Ben cases, the use of only the $4.3 \mu\text{m}$ CO_2 line
 268 overestimates the predicted numbers, especially for the 1 bar CO_2 case. Note that the reason why the overall required
 269 number of JWST observed transits is higher for the Hab scenarios is directly due to the presence of clouds that raised
 270 the continuum level up to the cloud deck altitude, shrinking each absorption line from the bottom and therefore
 271 reducing their detectability. This can clearly be seen in Fig. 7 where the left panels show the Ben 1 simulations and
 272 the right panels the Hab 1 simulations displaying a change in the continuum level. That change is significantly larger
 273 for ExoCAM, which has higher clouds, than UM. We can also see in Fig. 7 that 1 and 4 transits (green and magenta
 274 error bars, respectively) are far from being enough to detect the CO_2 features at $5\text{-}\sigma$ but that 20 transits (blue error
 275 bars) may be enough for Ben 1, while 40 transits (red error bars) may be necessary for Hab 1. Finally, we can also see
 276 that for the Hab 1 cases, water lines around $1.4 \mu\text{m}$ are too small to be detectable, even for the UM showing stronger
 277 H_2O lines due to its lower cloud deck.

278 The differences between the predicted transits from each GCM terminator atmosphere is to the first order control
 279 by the altitude of the cloud deck and to the second order by the T/P profile. Those differences between ExoCAM and

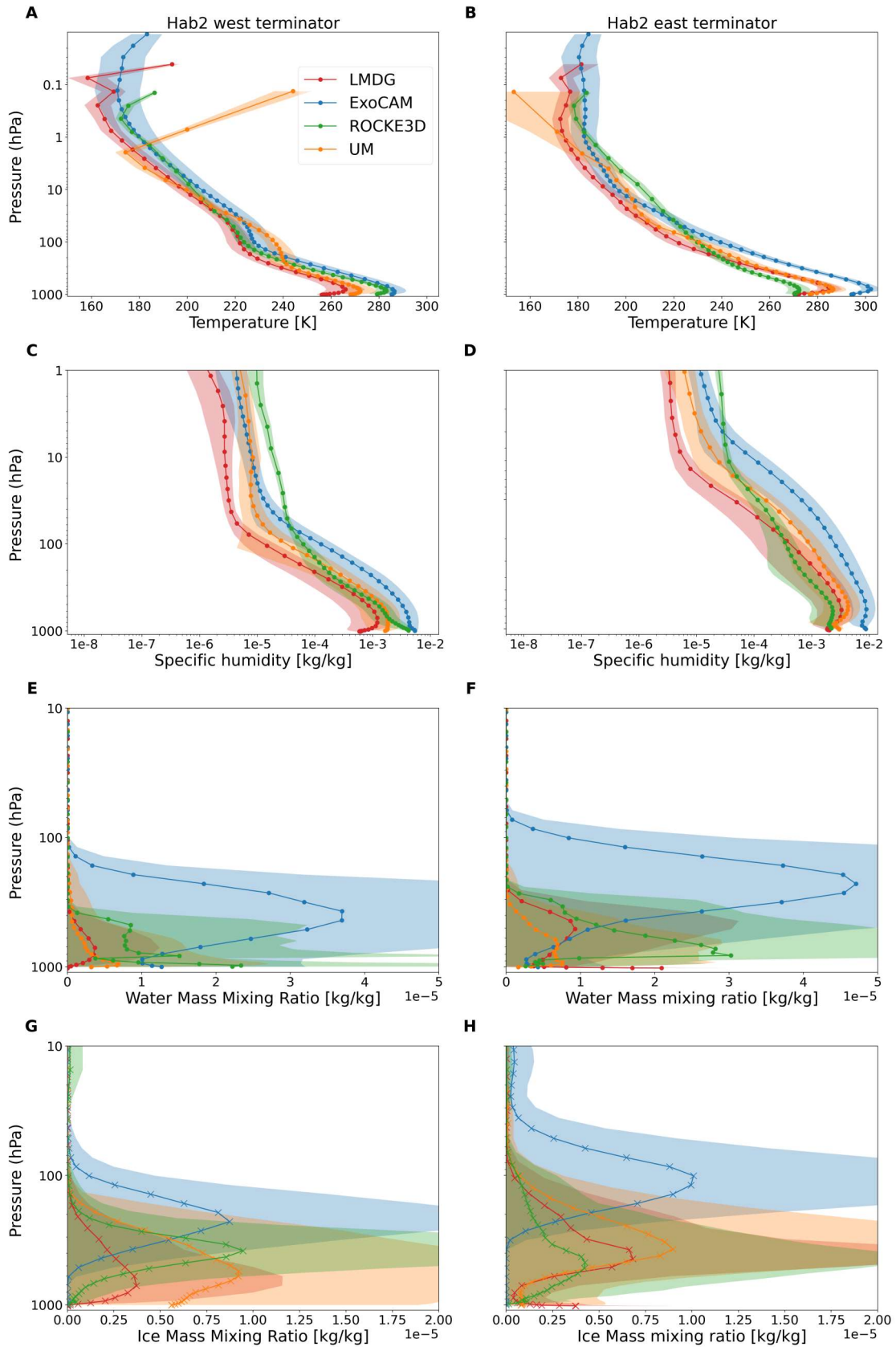


Figure 6. Hab 2 terminator atmospheric profiles simulated by ExoCAM (blue), LMD-G (red), ROCKE-3D (green) and the UM (orange). From top to bottom: temperature, specific humidity, mass mixing ratio of liquid water and mass mixing ratio of ice water for the west terminator (left column) and east terminator (right column). Time averaged values are represented by thick lines while the $1\text{-}\sigma$ deviations are represented by shades.

LMD-G on one hand and ROCKE-3D and the UM on the other are significant and could have consequences for the number of hours requested for a JWST proposal and on the interpretation of future data using retrieval algorithms. However, it seems clear that regardless the GCM used to produce the atmospheric data, at least 7 transit observations would be required to detect at a $5\text{-}\sigma$ confidence level a high molecular weight atmosphere on TRAPPIST-1e with a cloudy sky. Note that during JWST Cycle 1, 4 transits with NIRSpec Prism will be observed as part of the Guaranteed Observation Time (GTO) program 1331 led by PI Nikole Lewis. On average, this would lead to a $2\text{-}\sigma$ detection for Hab 1 and a $3.4\text{-}\sigma$ detection for Hab 2 (see column S/N-4 of Table 1).

3.3. Inter-transit variability

Many previous modeling studies estimating the detectability of an exoplanet through transmission spectroscopy have assumed that each planetary transit will be constant through time (Fauchez et al. 2019; Lustig-Yaeger et al. 2019; Komacek et al. 2020; Pidhorodetska et al. 2020; Suissa et al. 2020a,b). However, this is not a realistic assumption as weather patterns and clouds, if present, are likely to change from one transit to another. Previous work on hot Jupiters by Komacek & Showman (2019) has shown that temporal variability could be already detectable using either secondary eclipse observations with JWST or phase curve observations, and/or Doppler wind speed measurements with high-resolution spectrographs. More recently, May et al. (2021) simulated TRAPPIST-1e with ExoCAM for various concentration of CO_2 and looked at the atmospheric variability between 10 transits induced by ice water clouds. The amplitude of the transit variability for their 10^{-4} bar of CO_2 (comparable to Hab 1) and 1 bar CO_2 (comparable to Hab 2) are very similar, of the order of 10 and 20 ppm (May et al. 2021, their Fig. 4), respectively. However, they computed one transmission spectrum per day while in our study we compute it at the exact time of the transit, i.e. every 6.1 days, potentially leading to larger atmospheric differences. The main conclusion is that the time variability of the spectra does not affect retrieved abundances at detectable levels. However, the findings of May et al. (2021) are likely to be dependent on the GCM (ExoCAM). Here, we analyze the inter-transit variability produced by three more GCMs: LMD-G, ROCKE-3D and the UM.

Fig. 8 shows the standard deviation of the atmospheric transit depth and of the transit atmospheric thickness over 100 transits. This variability is wavelength dependent: it is the largest in the continuum as the transmitted light is closer to the surface, where clouds are present; and the smallest for the strongest absorption lines like the CO_2 at 2.7, 4.3 and $15\ \mu\text{m}$. There are significant differences between the GCMs. In general, the cloudier the simulation is, the more variable the transmission spectrum is. For LMD-G and ROCKE-3D, the time variability in both Hab 1 and Hab 2 is remarkably similar, while for ExoCAM and the UM it differs. This difference is due to the change in the average altitude of clouds between Hab 1 (Figure 4) and Hab 2 (Figure 6). In LMD-G and ROCKE-3D simulations, the average altitude of liquid water and ice water clouds does not change substantially between Hab 1 and Hab 2, while for ExoCAM and the UM it increases sharply in Hab 2. For instance, for ExoCAM the east terminator water ice clouds maximum density peaks at 500 hPa for Hab 1 and at 250 hPa for Hab 2. We hypothesise that stronger winds at this lower pressure relative to those deeper in the atmosphere lead to higher cloud variability. Overall, the standard deviation of the continuum level in the Hab 1 case for ExoCAM, LMD-G, ROCKE-3D and the UM is about 3, 3, 2 and 1 ppm, respectively, leading to a median value of ~ 2 ppm. For Hab 2 it is about 5, 3, 2.5 and 2 ppm, respectively, leading to a median value of ~ 3 ppm. These values are low relative to the JWST expected $1\text{-}\sigma$ noise of 10 to 25 ppm as assumed in Fauchez et al. (2019) and near the upper limit value (14 ppm) estimated by NIRSpec lab time series in Rustamkulov et al. (2022). It is also interesting to note that those values are comparable to the relative transit depth of H_2O or O_2 (Fauchez et al. 2019; Lustig-Yaeger et al. 2019; Pierrehumbert 2010; Wunderlich et al. 2020). This means that even if one assumes no noise floor, atmospheric variability would produce a continuum fluctuation that would swamp those highly important but weak absorption lines.

Fig. 9 shows the spectra as the ratio in percentage of the standard deviation of the variability with respect to the measurement noise for 100 (blue), 50 (orange), 25 (green) and 10 (red) transits for the atmospheric transit depth (left Y axis) and atmospheric thickness (right Y axis). The larger the number of transits, the lower the noise and therefore the higher the variability-to-noise ratio (%). Interestingly, these spectra can be reminiscent of emission spectra (Morley et al. 2017; Lustig-Yaeger et al. 2019; Fauchez et al. 2019). The minimum values correspond to the absorption line peak, while the maxima correspond to the continuum. Only the Hab 2 atmosphere simulated by ExoCAM would lead to a transit depth and atmospheric thickness variability higher than the measurements noise if 100 transits or more are acquired with JWST. Considering observation constraints and science priority this number is likely too high. Fauchez et al. (2019) have used the https://exoctk.stsci.edu/contam_visibility tool to estimate the number of times

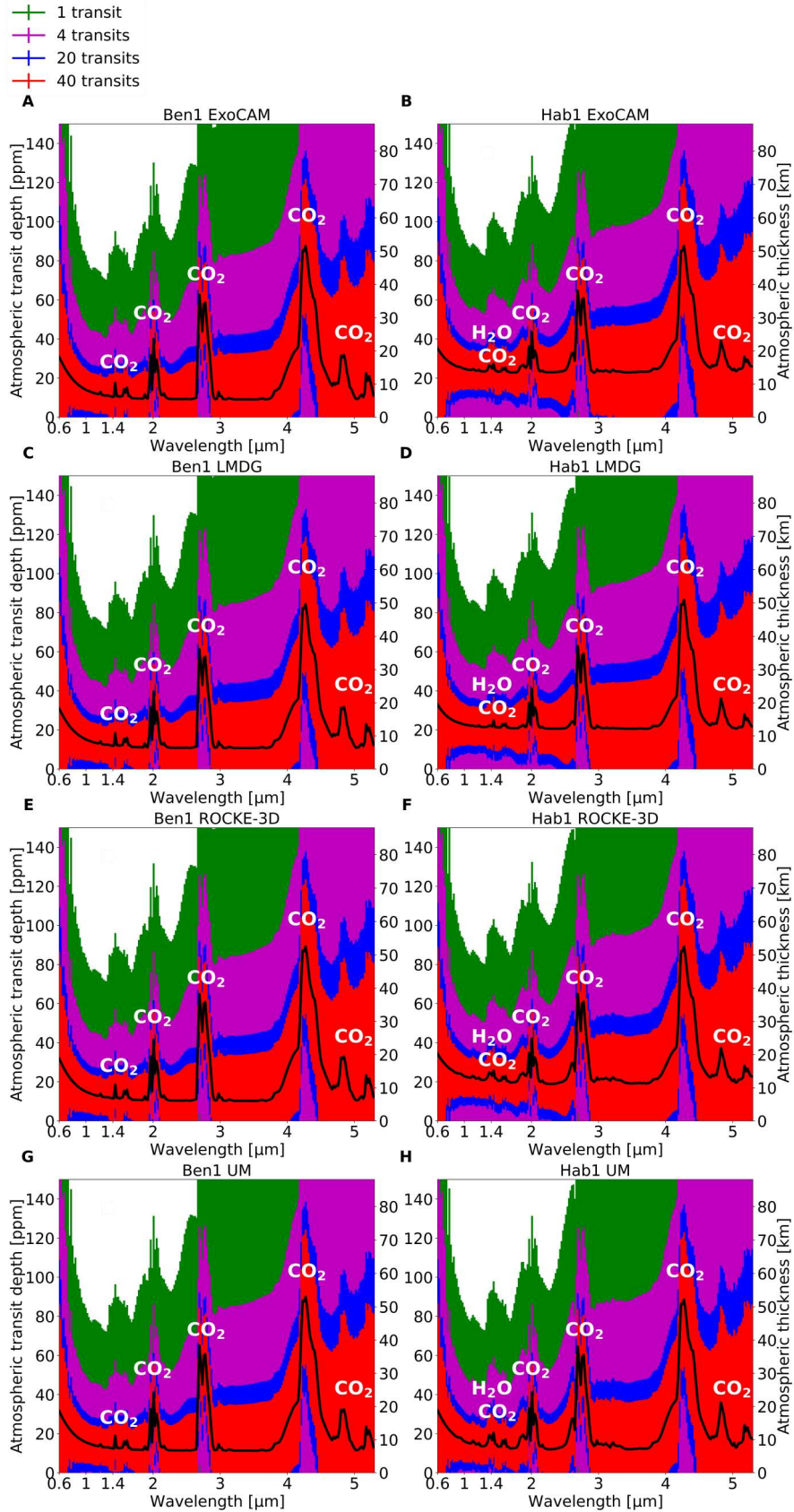


Figure 7. Ben 1 (left column) and Hab 1 (right column) transmission spectra for ExoCAM (A and B panels), LMD-G (C and D panels), ROCKE-3D (E and F panels) and UM (G and H panels). The error bars are shown for the native NIRSpec spectral resolution and for 1 transit (green), 4 transits (magenta, NIRSpec Cycle 1 proposal 1331 (Lewis et al. 2017)), 20 transits (blue, ~ 5 JWST years at a constant 4 transits per year) and 40 transits (red, ~ 10 JWST years at a constant 4 transits per year). Relevant absorption features are written in white.

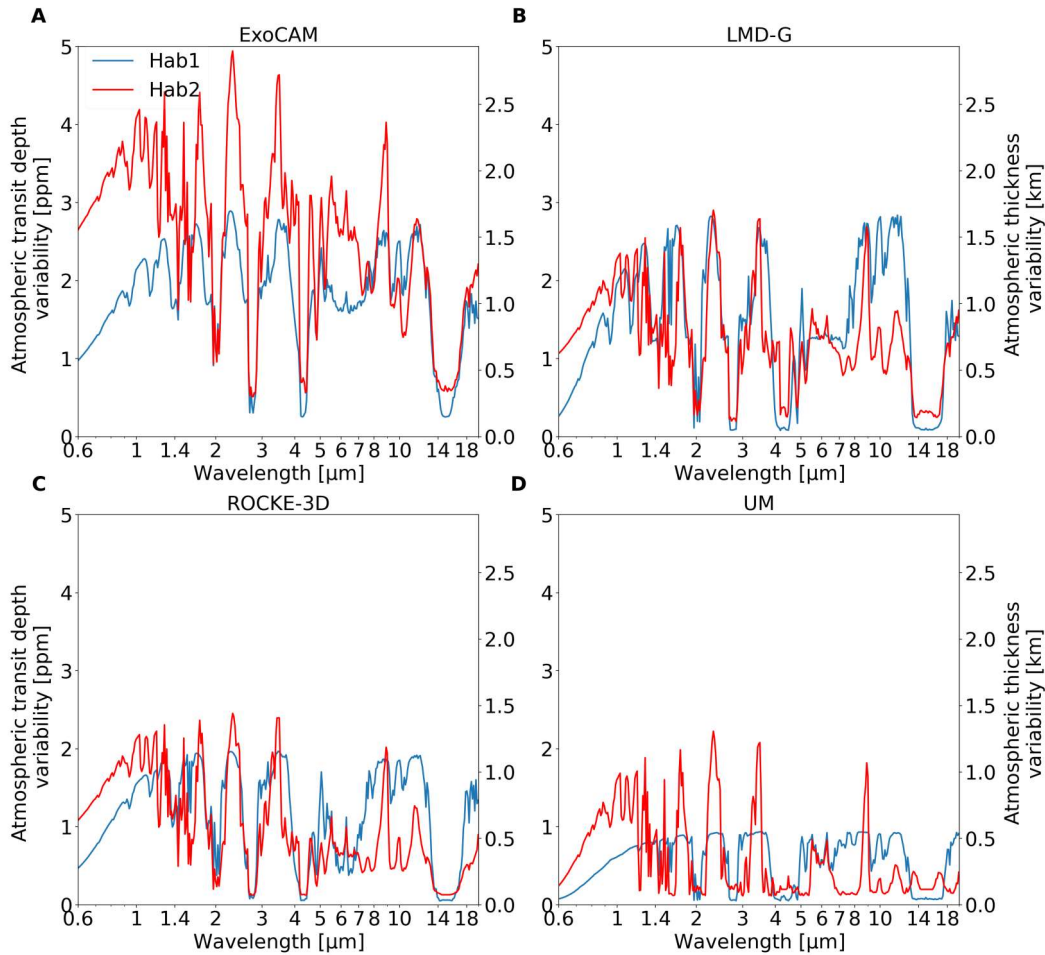


Figure 8. Standard deviation of the atmospheric transit depth [ppm] and of the atmospheric thickness [km] as a function of wavelength for Hab 1 (blue) and Hab 2 (red) and for ExoCAM (panel A), LMD-G (panel B), ROCKE-3D (panel C) and the UM (panel D).

331 TRAPPIST-1e will be visible transiting over JWST 5 years of nominal life time and found 85 (17 transit per year).
 332 The recent successful launch of JWST and optimized Ariane V trajectory saving large amounts of fuel has allowed us
 333 to extrapolate JWST lifetime up to 20 years. If every single transit is effectively observed this is an upper limit of 340
 334 available transits. However for Cycle 1, only 4 transits are going to be observed, if we assume that number constant
 335 over 20 years it will bring up to 80 transits. In our work, we have therefore considered 50 non-consecutive transits as
 336 a realistic but conservative estimate. In a more realistic scenario of 50 non-consecutive transits accumulated over the
 337 lifetime of the JWST, the impact of atmospheric variability relative to the noise for Hab 1 and Hab 2 would be of
 338 about 50% and 80% for ExoCAM, 50% and 50% for LMD-G, 40% and 40% for ROCKE-3D and 20% and 40% for the
 339 UM, respectively, and will therefore not be of a concern.

340 Comparisons between all GCMs in a single panel is shown in Fig. 10. In panels A (Hab 1) and B (Hab 2) are shown
 341 each ExoCAM transmission spectrum (black lines) and the median spectrum (blue line) with the associated 1-sigma
 342 error (blue error bars). ExoCAM was selected for this example as it is the GCM showing the largest variability. In
 343 panels C (Hab 1) and D (Hab 2) the spectra of the variability relative to noise for 50 transits and for the four GCMs
 344 are shown.

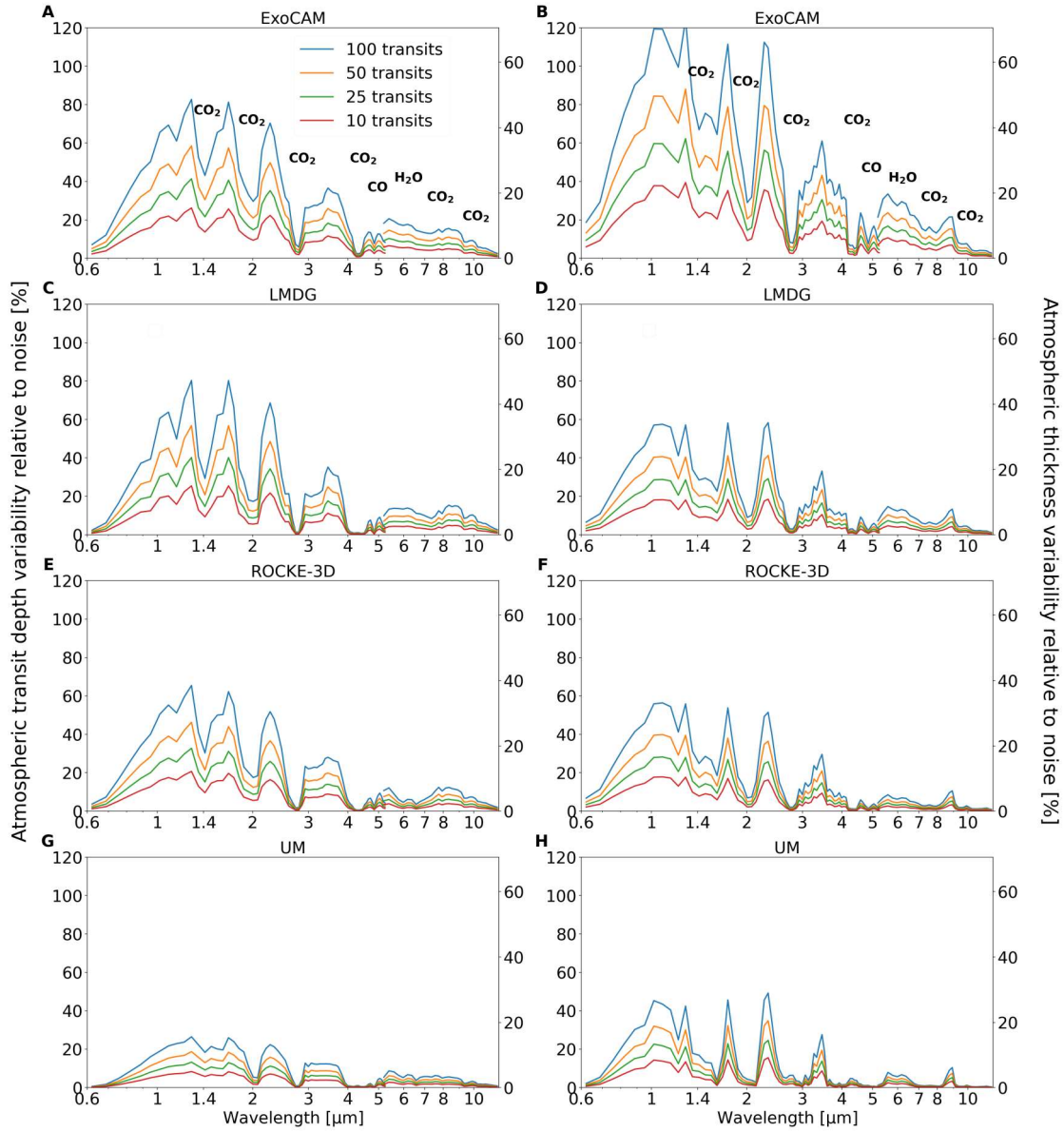


Figure 9. Atmospheric transit depth variability relative to noise (left Y axis) and atmospheric thickness variability relative to noise (right Y axis) for 100 (blue), 50 (orange), 25 (green) and 10 (red) transits for ExoCAM (panels A and B), LMD-G (panels C and D), ROCKE-3D (panels E and F) and the UM (panels G and H). Hab 1 is on the left column, Hab 2 on the right column. The noise is computed at the native instrument resolution and later binned down by a factor 3 for this figure.

345 As a summary, in the case of TRAPPIST-1e it seems predictions of the atmospheric variability introduced by clouds
 346 for an N₂ or CO₂-dominated atmosphere are within the measurements noise for a reasonable number of transits (< 50)
 347 regardless of the GCM used to simulate this temporal and spatial variability. However, if in the fortunate event (albeit
 348 unlikely; see the discussion in Gillon et al. 2020) that a similar exoplanet were to be found closer to Earth, the noise
 349 will be reduced. In that case the atmospheric variability could be a possible proxy for the presence of clouds via
 350 the temporal changes of the continuum level relative to the relatively stationary strong absorption peaks. Without
 351 such variability, a continuum level corresponding to a cloud deck, an atmospheric refraction limit or a planet's surface
 352 may not be discernible. Additionally, ExoCAM simulations produce systematically higher variability in the synthetic
 353 spectra compared to that in the three other models, while the UM tends to produce the lowest variability. LMD-G and
 354 ROCKE-3D are in the middle. We recommend that these differences in variability are taken into account when using a

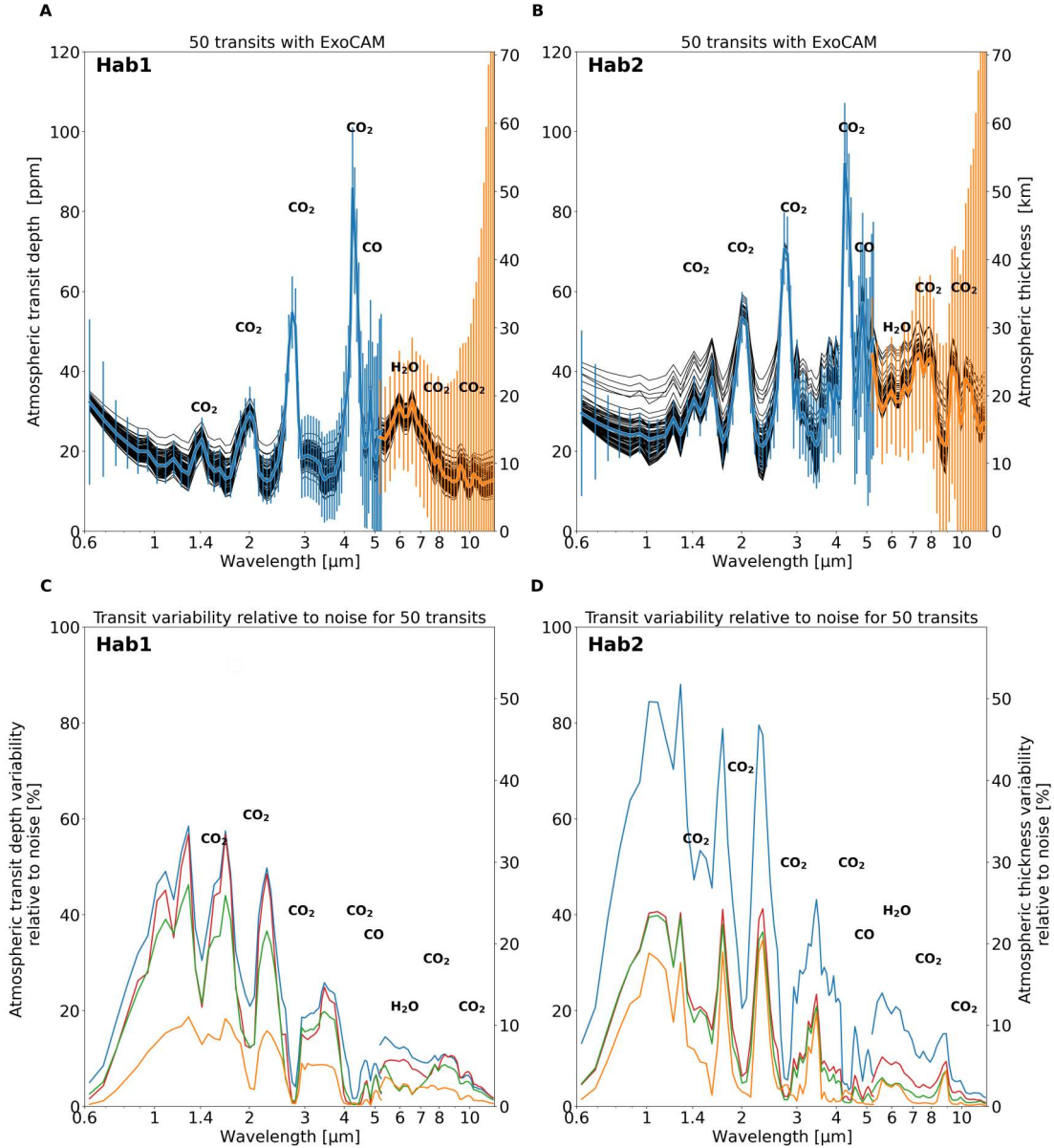


Figure 10. Panels A and B: transmission spectra for Hab 1 and Hab 2, respectively, obtained from ExoCAM simulations. Each fine black trace represents 1 of the 100 individual transits and the thick blue line represent the median transit. The noise for 50 transits and for both NIRSpect Prism (blue) and MIRI (orange) has been binned down by a factor 3 to maximize the number of photons per spectral bin while preserving the line shapes and is represented by the vertical error bars. Panels C and D: Hab 1 and Hab 2, respectively, atmospheric transit depth variability relative to noise (left Y axis) and atmospheric thickness variability relative to noise (right Y axis) for 50 transits and each of the four GCMs.

355 single GCM for future studies. Finally, [Sergeev et al. \(2021\)](#) have noticed that the time scale of this periodic variability
 356 differs between the models (see their Fig. 11). The tendency being the same for Hab 1 and Hab 2 with ExoCAM
 357 showing the longest period of 12.5 orbits for both cases, followed by LMD-G with 11.1 and 7.7 orbits, respectively,
 358 ROCKE-3D with 2.3 and 3 orbits, respectively and UM with 1.1 and 2.5 orbits, respectively. With real atmospheric
 359 data it is unknown what this period would be within this 1 to 12.5 orbit range. As a result, it is not clear if observing
 360 consecutive transits or scattered ones would have any impact on the atmospheric characterization. Finally, it is worth
 361 noting that while TRAPPIST-1e lies between the fast and Rhines rotation regimes ([Turbet et al. 2021](#); [Sergeev et al.](#)
 362 [2021](#)), planets with longer orbital periods that remain in synchronous rotation will transition from the Rhines rotation

regime to a slow rotation regime, which increases the symmetry of temperature and winds about the substellar point (Haqq-Misra et al. 2018), likely reducing even more the atmospheric variability across transits.

4. CONCLUSIONS

In this third and last part of the THAI paper series we analyzed how the prediction of the detectability of N_2 and CO_2 -dominated atmospheres on TRAPPIST-1e is sensitive to the choice of a 3D GCM used to simulate its atmosphere.

First, we have simulated the transmission spectra for the Ben 1 & Ben 2 scenarios (dry land planets for which the comparison of the predicted atmosphere is presented in Part I Turbet et al. (2021)) using the Planetary Spectrum Generator (PSG, Villanueva et al. (2018)). We have shown that the predicted spectra are similar between the GCMs and the number of transits to detect an atmosphere with a $5\text{-}\sigma$ confidence level is close the for Ben 1 (within 4 transits or 24 %) and Ben 2 (within 2 transits or 33 %) cases.

Concerning the aquaplanet scenarios, presented in Part II (Sergeev et al. 2021) of this work, we shown that in the terminator region, in the Hab 1 case, the ExoCAM water cloud mixing ratio (only true for liquid water) and altitude of the cloud deck are much higher than for LMD-G, ROCKE-3D and the UM, in that order. In the Hab 2 case, ExoCAM has on average higher thick clouds, followed by ROCKE-3D, and closely by LMD-G and finally the UM, with the relative difference between the three latter models being smaller than for the Hab 1 case. The large cloud mixing ratio for LMD-G was at first counter-intuitive as it employs a convective adjustment that notoriously produces less convective clouds than the mass-flux scheme used by the three other models, as also shown in (Yang et al. 2013; Sergeev et al. 2021). Here, at the terminator, the fact that LMD-G is cloudier than ROCKE-3D and UM is likely due to a larger production of stratiform clouds. Unfortunately, the THAI protocol did not include a differentiation between convective and stratiform clouds. This differentiation will be investigated in a future study.

The differences in the simulated cloud coverage between the models, along with changes in T/P and water vapor profile lead to 41 to 56% differences between the number of transits predicted to detect (at $5\text{-}\sigma$) molecular species in Hab 1 and Hab 2 cases, respectively, using the atmospheric profile of a GCM or another. These differences are non-negligible as they can change about $1 - \sigma$ the confidence level of a predicted detectability of an atmosphere or increase the observing time by 41 to 56%, potentially making a given observation proposal unfeasible. Without observational data, we do not know which model is closer to the truth, but comparing them against each other indicates whether the detectability estimate is optimistic or pessimistic. This work therefore provides for the first time a “GCM uncertainty error bar” of $\sim 50\%$ that needs to be considered in future analysis of JWST spectra of TRAPPIST-1e. Namely, simulations of temperate rocky exoplanets with ExoCAM would likely produce higher and thicker clouds relative to other GCMs. As a result, a tool like PSG would give a higher number of transits required to detect such an atmosphere. On the other hand, using ROCKE-3D or the UM would give a lower number of transits, because they would likely produce lower and thinner clouds. As for LMD-G, the number would be comparable to that of ExoCAM due to LMD-G’s colder upper atmosphere. It also seems that these relative differences increase with the atmospheric concentration of the gas (here CO_2) that is being retrieved. This is because more minor lines appear and as they are shallow they are more sensitive to the cloud properties predicted by a given GCM. However, a larger gas concentration generally lead to an lower average absolute number of transits. Note that with the 4 transits expected for NIRSpec Prism in the JWST Guaranteed Observation Time (GTO, program 1331, PI Nikole Lewis), we can expect an average of 2.6 and $4.3 - \sigma$ for the dry atmospheres Ben 1 and Ben 2 and an average of 2.0 and 3.4σ for the moist and cloudy Hab 1 and Hab 2 atmospheres, respectively.

THAI has been well received by the community, as demonstrated by the attendance of 125 people at the THAI workshop and the 35 authors of the THAI workshop report (Fauchez et al. 2021). Due to extreme paucity of observational data it is important for the exoplanet community to develop and maintain intercomparison frameworks to benchmark atmospheric models, improve physical parameterizations and evaluate their sensitivity. In this context, THAI is the first step toward a larger framework of intercomparison for exoplanets, the Climates Using Interactive Suites of Intercomparisons Nested for Exoplanet Studies (CUISINES). Within the CUISINES framework, we hope to develop intercomparison projects similar to THAI for exoplanets other than TRAPPIST-1e using an hierarchy of numerical models. Ultimately, the goal of CUISINES is to provide the exoplanet community, both on the modelling and observational ends of the spectrum, with model benchmarks and recommendations for comparison with existing observations and for planning future ones.

ACKNOWLEDGMENTS

T.J.F., G.L.V. and M.J.W. acknowledge support from the GSFC Sellers Exoplanet Environments Collaboration (SEEC), which is funded in part by the NASA Planetary Science Divisions Internal Scientist Funding Model. D.E.S., I.A.B., J.M. and N.J.M. acknowledge use of the Monsoon system, a collaborative facility supplied under the Joint Weather and Climate Research Programme, a strategic partnership between the Met Office and the Natural Environment Research Council. We acknowledge support of the Met Office Academic Partnership secondment program. This work was partly supported by a Science and Technology Facilities Council Consolidated Grant (ST/R000395/1), UKRI Future Leaders Fellowship (MR/T040866/1), and the Leverhulme Trust (RPG-2020-82).

This project has received funding from the European Union’s Horizon 2020 research and innovation program under the Marie Skłodowska-Curie Grant Agreement No. 832738/ESCAPE. M.T. thanks the Gruber Foundation for its generous support to this research. M.T. acknowledges support from the PORTAL BRAIN-be 2.0 BELSPO project. M.T. was granted access to the High-Performance Computing (HPC) resources of Centre Informatique National de l’Enseignement Supérieur (CINES) under the allocations N° A0020101167 and A0040110391 made by Grand Équipement National de Calcul Intensif (GENCI). This work has been carried out within the framework of the National Centre of Competence in Research PlanetS supported by the Swiss National Science Foundation. M.T. acknowledges the financial support of the SNSF. M.T. and F.F. thank the LMD Generic Global Climate team for the teamwork development and improvement of the model. J.H.M. acknowledges funding from the NASA Habitable Worlds program under award 80NSSC20K0230.

The authors thank the two anonymous reviewers whose comments helped to improve the quality and clarity of this manuscript. The authors acknowledge the help of Andrew Ackerman to set up the cloud diagnostics in ROCKE-3D. T.F. thank Avi. Mandell for his helpful discussion on the observation noise. The THAI GCM intercomparison team is grateful to the Anong’s THAI Cuisine restaurant in Laramie for hosting its first meeting on November 15, 2017. Numerical experiments performed for this study required the use of supercomputers, which are energy intensive facilities and thus have non-negligible greenhouse gas emissions associated with them.

Software: MATPLOTLIB (Hunter 2007). PSG (Villanueva et al. 2018) is available online at <https://psg.gsfc.nasa.gov/index.php>. ExoCAM (Wolf & Toon 2015) is available on Github: <https://github.com/storyofthewolf/ExoCAM>. The Met Office Unified Model is available for use under licence; see <http://www.metoffice.gov.uk/research/modelling-systems/unified-model>. ROCKE-3D is public domain software and available for download for free from <https://simplex.giss.nasa.gov/gcm/ROCKE-3D/>. Annual tutorials for new users take place annually, whose recordings are freely available on line at https://www.youtube.com/user/NASAGISStv/playlists?view=50&sort=dd&shelf_id=15. LMD-G is available upon request from Martin Turbet (martin.turbet@lmd.jussieu.fr) and François Forget (francois.forget@lmd.jussieu.fr).

APPENDIX

A. DATA ACCESSIBILITY

All our GCM THAI data are permanently available for download here: <https://ckan.emac.gsfc.nasa.gov/organization/thai>, with variables described for each dataset. If you use those data please cite this current paper and add the following statement: "THAI data have been obtained from <https://ckan.emac.gsfc.nasa.gov/organization/thai>, a data repository of the Sellers Exoplanet Environments Collaboration (SEEC), which is funded in part by the NASA Planetary Science Divisions Internal Scientist Funding Model."

Scripts to process the THAI data are available on GitHub: <https://github.com/projectcuisines>

Scripts to generate PSG/GlobES spectra are available on GitHub: <https://github.com/nasaps/globes>.

REFERENCES

- | | |
|---|--|
| <p>428 Agol, E., Dorn, C., Grimm, S. L., et al. 2021, The
 429 Planetary Science Journal, 2, 1, doi: 10.3847/PSJ/abd022
 430 Amundsen, D. S., Mayne, N. J., Baraffe, I., et al. 2016,
 431 A&A, 595, A36, doi: 10.1051/0004-6361/201629183</p> | <p>432 Batalha, N. E., Lewis, N. K., Line, M. R., Valenti, J., &
 433 Stevenson, K. 2018, The Astrophysical Journal, 856, L34,
 434 doi: 10.3847/2041-8213/aab896</p> |
|---|--|

- 435 Boutle, I. A., Joshi, M., Lambert, F. H., et al. 2020, *Nature* 484
 436 *Communications*, 11, 2731, 485
 437 doi: [10.1038/s41467-020-16543-8](https://doi.org/10.1038/s41467-020-16543-8) 486
- 438 Boutle, I. A., Mayne, N. J., Drummond, B., et al. 2017, 487
 439 *Astronomy & Astrophysics*, 601, A120, 488
 440 doi: [10.1051/0004-6361/201630020](https://doi.org/10.1051/0004-6361/201630020) 489
- 441 de Wit, J., Wakeford, H. R., Gillon, M., et al. 2016, *Nature* 490
 442 537, 69 EP . <https://doi.org/10.1038/nature18641> 491
- 443 de Wit, J., Wakeford, H. R., Lewis, N. K., et al. 2018, 492
 444 *Nature Astronomy*, 2, 214, 493
 445 doi: [10.1038/s41550-017-0374-z](https://doi.org/10.1038/s41550-017-0374-z) 494
- 446 Douglas, E. S., Ashcraft, J. N., Belikov, R., et al. 2020, 495
 447 *Space Telescopes and Instrumentation 2020: Optical,* 496
 448 *Infrared, and Millimeter Wave*, doi: [10.1117/12.2561960](https://doi.org/10.1117/12.2561960) 497
- 449 Fauchez, T. J., Turbet, M., Villanueva, G. L., et al. 2019, 498
 450 *ApJ*, 887, 194, doi: [10.3847/1538-4357/ab5862](https://doi.org/10.3847/1538-4357/ab5862) 499
- 451 Fauchez, T. J., Turbet, M., Wolf, E. T., et al. 2020a, 500
 452 *Geoscientific Model Development*, 13, 707, 501
 453 doi: [10.5194/gmd-13-707-2020](https://doi.org/10.5194/gmd-13-707-2020) 502
- 454 Fauchez, T. J., Villanueva, G. L., Schwieterman, E. W., 503
 455 et al. 2020b, *Nature Astronomy*, 1 504
- 456 Fauchez, T. J., Turbet, M., Sergeev, D. E., et al. 2021, *The* 505
 457 *Planetary Science Journal*, 2, 106, 506
 458 doi: [10.3847/PSJ/abf4df](https://doi.org/10.3847/PSJ/abf4df) 507
- 459 Gaudi, B. S., Seager, S., Mennesson, B., et al. 2018, *arXiv* 508
 460 e-prints, arXiv:1809.09674. 509
 461 <https://arxiv.org/abs/1809.09674> 510
- 462 Gillon, M., Jehin, E., Lederer, S. M., et al. 2016, *Nature*, 511
 463 533, 221 . <https://doi.org/10.1038/nature17448> 512
- 464 Gillon, M., Triaud, A. H. M. J., Demory, B.-O., et al. 2017, 513
 465 *Nature*, 542, 456–460. 514
 466 <https://doi.org/10.1038/nature21360> 515
- 467 Gillon, M., Meadows, V., Agol, E., et al. 2020, *The* 516
 468 *TRAPPIST-1 JWST Community Initiative*. 517
 469 <https://arxiv.org/abs/2002.04798> 518
- 470 Gordon, I., Rothman, L., Hargreaves, R., et al. 2022, 519
 471 *Journal of Quantitative Spectroscopy and Radiative* 520
 472 *Transfer*, 277, 107949, 521
 473 doi: <https://doi.org/10.1016/j.jqsrt.2021.107949> 522
- 474 Grimm, S. L., Demory, B.-O., Gillon, M., et al. 2018, 523
 475 *Astronomy & Astrophysics*, 613, A68, 524
 476 doi: [10.1051/0004-6361/201732233](https://doi.org/10.1051/0004-6361/201732233) 525
- 477 Haqq-Misra, J., Wolf, E. T., Joshi, M., Zhang, X., & 526
 478 Kopparapu, R. K. 2018, *The Astrophysical Journal*, 852, 527
 479 67, doi: [10.3847/1538-4357/aa9f1f](https://doi.org/10.3847/1538-4357/aa9f1f) 528
- 480 Hori, Y., & Ogihara, M. 2020, *ApJ*, 889, 77, 529
 481 doi: [10.3847/1538-4357/ab6168](https://doi.org/10.3847/1538-4357/ab6168) 530
- 482 Hunter, J. D. 2007, *Computing in Science & Engineering*, 9, 530
 483 90, doi: [10.1109/MCSE.2007.55](https://doi.org/10.1109/MCSE.2007.55) 531
- Kane, S. R., Jansen, T., Fauchez, T., Selsis, F., & Ceja, 532
 A. Y. 2021, *The Astronomical Journal*, 161, 53, 533
 doi: [10.3847/1538-3881/abcfbe](https://doi.org/10.3847/1538-3881/abcfbe) 534
- Karman, T., Gordon, I. E., van der Avoird, A., et al. 2019, 535
Icarus, 328, 160, doi: [10.1016/j.icarus.2019.02.034](https://doi.org/10.1016/j.icarus.2019.02.034) 536
- Keller-Rudek, H., Moortgat, G. K., Sander, R., & Sørensen, 537
 R. 2013, *Earth System Science Data*, 5, 365, 538
 doi: [10.5194/essd-5-365-2013](https://doi.org/10.5194/essd-5-365-2013) 539
- Kofman, V., & Villanueva, G. L. 2021, *JQSRT*, 270, 540
 107708, doi: [10.1016/j.jqsrt.2021.107708](https://doi.org/10.1016/j.jqsrt.2021.107708) 541
- Koll, D. D. B., & Abbot, D. S. 2016, *The Astrophysical* 542
Journal, 825, 99, doi: [10.3847/0004-637x/825/2/99](https://doi.org/10.3847/0004-637x/825/2/99) 543
- Koll, D. D. B., Malik, M., Mansfield, M., et al. 2019, *ApJ*, 544
 886, 140, doi: [10.3847/1538-4357/ab4c91](https://doi.org/10.3847/1538-4357/ab4c91) 545
- Komacek, T. D., Fauchez, T. J., Wolf, E. T., & Abbot, 546
 D. S. 2020, *The Astrophysical Journal*, 888, L20, 547
 doi: [10.3847/2041-8213/ab6200](https://doi.org/10.3847/2041-8213/ab6200) 548
- Komacek, T. D., & Showman, A. P. 2019, *The* 549
Astrophysical Journal, 888, 2, 550
 doi: [10.3847/1538-4357/ab5b0b](https://doi.org/10.3847/1538-4357/ab5b0b) 551
- Kopparapu, R. K., Ramirez, R., Kasting, J. F., et al. 2013, 552
The Astrophysical Journal, 765, 131. 553
<http://stacks.iop.org/0004-637X/765/i=2/a=131> 554
- Krishnamurthy, V., Hirano, T., Stefánsson, G., et al. 2021, 555
AJ, 162, 82, doi: [10.3847/1538-3881/ac0d57](https://doi.org/10.3847/1538-3881/ac0d57) 556
- Lewis, N., Clampin, M., Mountain, M., et al. 2017, *Transit* 557
Spectroscopy of TRAPPIST-1e, JWST Proposal. Cycle 1 558
- Lewis, N. T., Lambert, F. H., Boutle, I. A., et al. 2018, 559
ApJ, 854, 171, doi: [10.3847/1538-4357/aaad0a](https://doi.org/10.3847/1538-4357/aaad0a) 560
- Lin, Z., MacDonald, R. J., Kaltenegger, L., & Wilson, D. J. 561
 2021, *Monthly Notices of the Royal Astronomical* 562
Society, 505, 3562–3578, doi: [10.1093/mnras/stab1486](https://doi.org/10.1093/mnras/stab1486) 563
- Lincowski, A. P., Meadows, V. S., Crisp, D., et al. 2018, 564
ApJ, 867, 76, doi: [10.3847/1538-4357/aae36a](https://doi.org/10.3847/1538-4357/aae36a) 565
- Luger, R., Sestovic, M., Kruse, E., et al. 2017, *Nature* 566
Astronomy, 1, 0129, doi: [10.1038/s41550-017-0129](https://doi.org/10.1038/s41550-017-0129) 567
- Lustig-Yaeger, J., Meadows, V. S., & Lincowski, A. P. 2019, 568
The Astronomical Journal, 158, 27, 569
 doi: [10.3847/1538-3881/ab21e0](https://doi.org/10.3847/1538-3881/ab21e0) 570
- Massie, S. T., & Hervig, M. 2013, *JQSRT*, 130, 373, 571
 doi: [10.1016/j.jqsrt.2013.06.022](https://doi.org/10.1016/j.jqsrt.2013.06.022) 572
- May, E. M., Taylor, J., Komacek, T. D., Line, M. R., & 573
 Parmentier, V. 2021, *Water Ice Cloud Variability &* 574
Multi-Epoch Transmission Spectra of TRAPPIST-1e. 575
<https://arxiv.org/abs/2103.09313> 576
- Mayne, N. J., Baraffe, I., Acreman, D. M., et al. 2014, 577
Geoscientific Model Development, 7, 3059, 578
 doi: [10.5194/gmd-7-3059-2014](https://doi.org/10.5194/gmd-7-3059-2014) 579

- 532 Moran, S. E., Hörst, S. M., Batalha, N. E., Lewis, N. K., & 572
 533 Wakeford, H. R. 2018, *The Astronomical Journal*, 156, 573
 534 252. <http://stacks.iop.org/1538-3881/156/i=6/a=252> 574
- 535 Morley, C. V., Kreidberg, L., Rustamkulov, Z., Robinson, 575
 536 T., & Fortney, J. J. 2017, *The Astrophysical Journal*, 576
 537 850, 121, doi: [10.3847/1538-4357/aa927b](https://doi.org/10.3847/1538-4357/aa927b) 577
- 538 Pidhorodetska, D., Fauchez, T. J., Villanueva, G. L., 578
 539 Domagal-Goldman, S. D., & Kopparapu, R. K. 2020, *The* 579
 540 *Astrophysical Journal*, 898, L33, 580
 541 doi: [10.3847/2041-8213/aba4a1](https://doi.org/10.3847/2041-8213/aba4a1)
- 542 Pierrehumbert, R. T. 2010, *Principles of Planetary Climate* 581
- 543 Rustamkulov, Z., Sing, D., Liu, R., & Wang, A. 2022, 582
 544 Analysis of a JWST NIRSpec Lab Time Series: 583
 545 Characterizing Systematics, Recovering Exoplanet 584
 546 Transit Spectroscopy, and Constraining a Noise Floor. 585
 547 <https://arxiv.org/abs/2203.04173> 586
- 548 Selsis, F., Wordsworth, R. D., & Forget, F. 2011, *A&A*, 587
 549 532, A1, doi: [10.1051/0004-6361/201116654](https://doi.org/10.1051/0004-6361/201116654) 588
- 550 Sergeev, D. E., Fauchez, T. J., Turbet, M., et al. 2021, 589
 551 arXiv e-prints, arXiv:2109.11459. 590
 552 <https://arxiv.org/abs/2109.11459> 591
- 553 Sneep, M., & Ubachs, W. 2005, *Journal of Quantitative* 592
 554 *Spectroscopy and Radiative Transfer*, 92, 293, 593
 555 doi: <https://doi.org/10.1016/j.jqsrt.2004.07.025> 594
- 556 Suissa, G., Mandell, A. M., Wolf, E. T., et al. 2020a, *The* 595
 557 *Astrophysical Journal*, 891, 58, 596
 558 doi: [10.3847/1538-4357/ab72f9](https://doi.org/10.3847/1538-4357/ab72f9)
- 559 Suissa, G., Wolf, E. T., kumar Kopparapu, R., et al. 2020b, 597
 560 *The Astronomical Journal*, 160, 118, 598
 561 doi: [10.3847/1538-3881/aba4b4](https://doi.org/10.3847/1538-3881/aba4b4) 599
- 562 TheLUVOIRTeam. 2019. <https://arxiv.org/abs/1912.06219> 600
- 563 Turbet, M., Bolmont, E., Bourrier, V., et al. 2020, *Space* 601
 564 *Science Reviews*, 216, 100, 602
 565 doi: [10.1007/s11214-020-00719-1](https://doi.org/10.1007/s11214-020-00719-1) 603
- 566 Turbet, M., Leconte, J., Selsis, F., et al. 2016, *Astronomy* 604
 567 *& Astrophysics*, 596, A112, 605
 568 doi: [10.1051/0004-6361/201629577](https://doi.org/10.1051/0004-6361/201629577)
- 569 Turbet, M., Bolmont, E., Leconte, J., et al. 2018, 606
 570 *Astronomy & Astrophysics*, 612, A86, 607
 571 doi: [10.1051/0004-6361/201731620](https://doi.org/10.1051/0004-6361/201731620) 608
- Turbet, M., Fauchez, T. J., Sergeev, D. E., et al. 2021, 609
 arXiv e-prints, arXiv:2109.11457. 610
<https://arxiv.org/abs/2109.11457> 611
- Villanueva, G. L., Liuzzi, G., Faggi, S., et al. 2022, 612
 Fundamentals of the Planetary Spectrum Generator 613
- Villanueva, G. L., Smith, M. D., Protopapa, S., Faggi, S., & 614
 Mandell, A. M. 2018, *Journal of Quantitative* 615
Spectroscopy and Radiative Transfer, 217, 86, 616
 doi: [10.1016/j.jqsrt.2018.05.023](https://doi.org/10.1016/j.jqsrt.2018.05.023) 617
- von Paris, P., Gratier, P., Bordé, P., & Selsis, F. 2016, 618
A&A, 587, A149, doi: [10.1051/0004-6361/201526297](https://doi.org/10.1051/0004-6361/201526297) 619
- Warren, S. G. 1984, *ApOpt*, 23, 1206, 620
 doi: [10.1364/AO.23.001206](https://doi.org/10.1364/AO.23.001206) 621
- Way, M. J., Aleinov, I., Amundsen, D. S., et al. 2017, 622
Astrophys. J. Supp. Series, 231, 12, 623
 doi: [10.3847/1538-4365/aa7a06](https://doi.org/10.3847/1538-4365/aa7a06) 624
- Wolf, E. T., Kopparapu, R., Haqq-Misra, J., & Fauchez, 625
 T. J. 2021 626
- Wolf, E. T., Kopparapu, R. K., & Haqq-Misra, J. 2019, 627
ApJ, 877, 35, doi: [10.3847/1538-4357/ab184a](https://doi.org/10.3847/1538-4357/ab184a) 628
- Wolf, E. T., & Toon, O. B. 2015, *Journal of Geophysical* 629
Research: Atmospheres, 120, 5775, 630
 doi: [10.1002/2015JD023302](https://doi.org/10.1002/2015JD023302) 631
- Wordsworth, R. D., Forget, F., Selsis, F., et al. 2011, *The* 632
Astrophysical Journal Letters, 733, L48, 633
 doi: [10.1088/2041-8205/733/2/L48](https://doi.org/10.1088/2041-8205/733/2/L48) 634
- Wunderlich, F., Godolt, M., Grenfell, J. L., et al. 2019, 635
A&A, 624, A49, doi: [10.1051/0004-6361/201834504](https://doi.org/10.1051/0004-6361/201834504) 636
- Wunderlich, F., Scheucher, M., Godolt, M., et al. 2020, *The* 637
Astrophysical Journal, 901, 126, 638
 doi: [10.3847/1538-4357/aba59c](https://doi.org/10.3847/1538-4357/aba59c) 639
- Yang, J., Cowan, N. B., & Abbot, D. S. 2013, *The* 640
Astrophysical Journal, 771, L45, 641
 doi: [10.1088/2041-8205/771/2/L45](https://doi.org/10.1088/2041-8205/771/2/L45) 642
- Yang, J., Leconte, J., Wolf, E. T., et al. 2019, *The* 643
Astrophysical Journal, 875, 46, 644
 doi: [10.3847/1538-4357/ab09f1](https://doi.org/10.3847/1538-4357/ab09f1) 645